ROYAL SOCIETY OF CHEMISTRY

Check for updates

Modeling and admittance recursive simulation of anti-reflective coatings for photothermal conversion: synergy between subwavelength structures and gradient refractive index layers

Zihao Zhu,[a] Yanyan Bu*[c] and Xiangfu Wang [ID] *[ab]

In the field of photothermal conversion, light-absorbing layers show limitations such as low solar energy utilization and excessive surface reflection. This paper proposes a new anti-reflective coating consisting of a gradient-doped fluorescent glass film covering a subwavelength structural layer for photothermal conversion. Its transmittance was simulated using equivalent medium theory and the admittance recursion method. The subwavelength structure provides a refractive index gradient, and its shape solves the problem of the sharp decrease in transmittance at high angles of incidence. Subsequently, we adjust the material parameters of the gradient refractive layers and control the thickness of each layer to minimize interlayer Fresnel reflections. Finally, the efficient light-trapping ability of the model was verified by calculating and comparing the transmittances of the optimized model and bare glass. Notably, within the visible spectrum, our model achieves an average transmittance of over 95% across wavelength and angle ranges, effectively suppressing surface reflections. At a larger light incident angle, the transmittance increases by 29.7%, and the minimum angle transmittance reaches 92.7%. This study proposes an innovative method to enhance the performance of transmission layers in photothermal conversion devices.

1. Introduction

Solar energy is currently the cleanest and most environmentally friendly energy source. Photothermal conversion[1] is a seemingly primitive but effective method of utilizing solar energy, involving the capture of solar radiation through photothermal materials and converting it into thermal energy for use in a variety of beneficial applications. At present, solar energy is mainly utilized in photovoltaics,[2,3] photocatalysis[4] and photothermal conversion. Compared with the other two methods, photothermal conversion is simple, has a wide range of available materials, and has particularly high energy conversion efficiency. For example, Wen *et al.*[5] developed a silver nanofluid that can increase stored thermal energy by up to 144% at peak temperature. Guo *et al.*[6] demonstrated that ZrC has excellent photothermal conversion performance (24.06%) and can completely inactivate *E. coli* within 15 minutes. Zhang *et al.*[7]

prepared a variety of Cu_7S_4 in different shapes and irradiated them under infrared lamps, and the energy conversion efficiency reached 77.1%.

The main reason for choosing photothermal conversion as the research focus is its simplicity, strong material versatility and high energy conversion efficiency, which has higher research value. Photovoltaic power generation requires complex semiconductor materials and manufacturing processes[2] and photocatalysis usually involves complex catalytic systems;[4] photothermal conversion can be achieved with relatively simple and abundant materials. The high energy conversion efficiency of photothermal materials, such as the previously mentioned silver nanofluids, ZrC and Cu_7S_4, shows their potential for efficient use of solar energy. In addition, photothermal conversion extends from energy storage to practical applications such as steam generation,[8] where photothermal materials can quickly convert solar energy into steam for desalination and industrial processes. In solar distillation[9] this mechanism is used to purify water, providing a sustainable solution for water-scarce regions. In the medical field, photothermal materials are being explored for cancer treatment,[10] where local heating can destroy cancer cells with minimal side effects. These practical applications further reflect that the photothermal conversion has a certain research value.

[a] College of Electronic and Optical Engineering & College of Flexible Electronics (Future Technology), Nanjing University of Posts and Telecommunications, Nanjing 210023, China. E-mail: xfwang@njupt.edu.cn

[b] The State Key Laboratory of Refractories and Metallurgy (Wuhan University of Science and Technology), Wuhan 430081, China

[c] College of Science, Nanjing University of Posts and Telecommunications, Nanjing 210023, China. E-mail: buyy@njupt.edu.cn

This journal is © the Owner Societies 2024

Phys. Chem. Chem. Phys., 2024, **26**, 19755–19774 | **19755**

With progress in research, the development of photothermal conversion materials encounters significant challenges. Research on new composite materials is time-consuming, costly and requires rigorous preparation processes, making it difficult to produce them on a large scale. Therefore, in order to enhance the photothermal conversion efficiency, it is crucial to optimize the design of the light-transmitting layer during the photothermal conversion process. This optimization aims to solve the problems of high reflectivity, narrow absorption spectrum, and low solar energy utilization of photothermal materials.

Antireflective coatings[11–14] play an indispensable role in today's optical field and have been widely used in various types of optical equipment. In terms of light reflection suppression, the C–Si solar cell with the AR film designed by Tang et al.[3] showed excellent broadband suppression of surface light reflectance of 17.7%. Leem et al.[15] designed a parabolic AZO SWG structure that significantly reduced the maximum reflectance to less than 9.8% over a wide wavelength range of 300–1100 nm. In terms of light transmission enhancement, Florian Maudet et al.[16] designed anti-reflective coating double layers made via oblique angle deposition can achieve an ultra-high average transmittance of 98.97% over the broadband 400–1800 nm.

Among various anti-reflective coatings, subwavelength structures[17–22] and gradient refractive layers[23–27] are currently widely used. Hong Li et al.[28] prepared PiTG with a GRIN coating, revealing that compared to single refractive index (SRIN) coatings, the luminous efficiency of PiTG with the GRIN coating increased from 9.51% to 23.12%. Minkyu Choi et al.[29] added a MgF_2 coating based on the gradient refractive index on Si substrates, and the mean reflectance (R_{avg}) and solar weighted reflectance (R_{sw}) in the wide wavelength range of 350–1100 nm were 14% and 12.1%. Han et al.[30] studied porous polymer films coated with glass substrates, and the transmittance of these graded refractive index structures to visible light and near-infrared (NIR) light reached more than 97%.

Therefore, we opted to construct a gradient fluorescent glass transmission layer covered with a subwavelength structural coating as the transmission layer model for photothermal conversion, and used the admittance recursion method[31] and effective medium theory[32–34] to determine the shape, structural parameters and transmitted light characteristics of the model. In our previous article,[35,36] we have studied the synergistic anti-reflective coating of photothermal conversion. Based on our previous researches, this paper conducted further research in the following aspects: ① In the subwavelength structure layer, SnO_2 was doped into SiO_2 to reduce the interlayer Fresnel reflection. ② By splicing multiple models together, a new subwavelength structure model was designed, and the optimal shape was determined on the same scale. ③ The influence of the transverse electric wave (TE) and transverse magnetic wave (TM) of the incident light on the transmission performance of the model with the change of the incident angles was studied. ④ The influence of the thickness change of each layer in the gradient refractive layer on the light propagation process and light transmission performance was considered.

2. Modeling and simulation

2.1. Model and theory introduction

Drawing from the preceding investigation and research analysis, this study endeavors to devise an efficient anti-reflective coating for improving photothermal conversion efficiency to solve the problems of high reflectivity, narrow absorption spectrum, and low solar energy utilization. The anti-reflective coating consists of a subwavelength structure and three gradient refractive layers, which can be directly covered on the absorption layer of photothermal conversion to increase the light absorption rate, as shown in Fig. 1.

The first layer is a subwavelength structure layer made of $SnO_2 \cdot SiO_2$, which is used to receive incident light. When light travels from one medium to another, Fresnel reflection occurs due to a large discontinuity in the refractive index at the interface of the different media. This phenomenon has a negative impact on the transmission of light energy.[37] The subwavelength structure reduces the reflection of incident light by creating a gradient refractive index. Its main working principle is to construct an undulating structure with gradient changes in the structural scale along the direction of light incidence.[38–40] After a series of equivalent calculations, it can be transformed[41,42] as a film with gradient refractive index. At this time, since there is no abrupt interface, the Fresnel reflection phenomenon of incident light is greatly reduced, enhancing the light transmittance of the anti-reflective coating. This structure works by disrupting the optical path at the nanometer scale, effectively minimizing Fresnel reflections that typically occur at interfaces between different media.

In this study, we systematically explore the effects of various subwavelength structural parameters, such as shape and size, on antireflective properties. We studied shapes such as ellipses,[43] paraboloids,[15] cylinders,[44] cones[44,45] and pyramids,[46] with the initial height set to 550 nm and the arrangement period to 173 nm.[36] Among them, ellipses, cylinders, conics and rotating paraboloids are stacked with hexagons, and cubes and pyramids are stacked with square grids, as shown in Fig. 1(a)–(f). Through simulation calculations, the changing law of light transmittance of the corresponding structure is obtained. According to the calculation results, the initial subwavelength structure is combined and regulated, and continuously optimized to find the optimal subwavelength structure shape and height, as shown in Fig. 1(g) and (h).

Each shape is chosen based on its unique ability to refract light, aiming to find the best configuration that maximizes light transmission and minimizes reflection. In order to systematically study these structures, below we will perform simulation calculations using equivalent medium theory to determine the effective refractive index and extinction coefficient. This allows us to model these structures as multilayers and optimize their model appearance and structural dimensions through iterative calculations.

After the light passes through the subwavelength structural layer, it will be refracted to the gradient refractive layer. The photothermal performance of photoexcited materials is mainly affected by two aspects:[47] light capture ability and photothermal

19756 | *Phys. Chem. Chem. Phys.*, 2024, **26**, 19755–19774

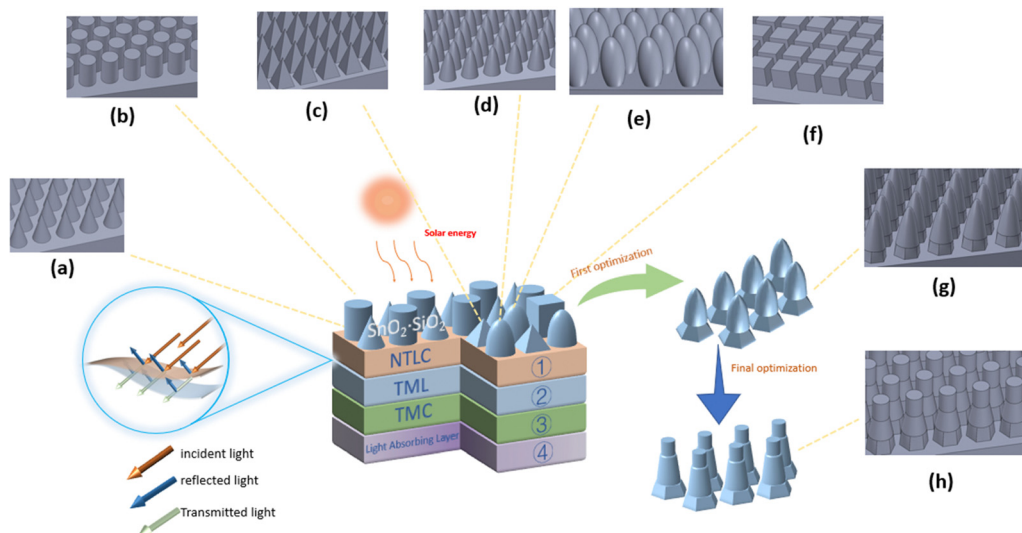This journal is © the Owner Societies 2024

Fig. 1 The physical model of the transmission layer of the photothermal conversion device, the amplification model of the periodic subwavelength structure and the schematic diagram of light propagation between layers.

conversion efficiency. Gradient refractive index (GRIN) can effectively improve the light harvesting capability of photothermal conversion devices. The gradient refractive index provides a smooth transition between different refractive indexes, which can effectively reduce reflection losses and enhance light absorption.[48] This is particularly beneficial in photothermal applications, where maximizing light absorption is critical for efficient heat generation. For traditional multilayer structures with a discrete refractive index, multilayer films may suffer from high reflection and limited wavelength absorption range due to sharp interfaces between layers. In contrast, the smooth refractive index transition of the GRIN layer provides lower reflectivity and broader wavelength absorption, minimizing reflection and allowing more light to be absorbed. Another significant advantage of GRIN layers is their ability to achieve broadband absorption.[49] The gradual refractive index transition allows efficient absorption of a wide range of wavelengths, making them ideal for solar photothermal applications where the light source consists of a broad spectrum. This feature ensures that most of the incident solar energy is absorbed and converted into heat, thereby increasing the overall efficiency of photothermal conversion.

The gradient refraction layer designed in this study has a total of four layers, all of which are positive planar structures. The first three layers are the gradient refraction part, and the fourth layer is the absorption layer for photothermal conversion. In Fig. 1, 1 represents the first gradient refractive layer, the material is $Nb_2O_5 \cdot 6Ta_2O_5 \cdot 3Li_2Si_2O_5 \cdot Ca_5(PO_4)_3F$, hereinafter referred to as NTLC. The initial thickness is 250 nm. 2 represents the second gradient refractive layer, the material is $4Ta_2O_5 \cdot MgF_2 \cdot Li_2Si_2O_5$, hereinafter referred to as TML, and its initial thickness is 50 nm. 3 represents the third gradient refractive layer, the material is $4Ta_2O_5 \cdot MgF_2 \cdot Ca_5(PO_4)_3F$, hereinafter referred to as TMC, and its initial thickness is 50 nm. Later, the transmission performance of the three gradient

refractive layers will be evaluated through the admittance recursion method, and the thickness of each layer will be changed for comparison to find a suitable thickness to improve the light absorption rate. 4 represents the absorption layer that accepts transmitted light for photothermal conversion. This article will use glass as a replacement to calculate the AR performance and optimization degree of the anti-reflective coating.

In the selection of materials for each layer of the anti-reflective coating, we choose ceramic glass materials with a stable refractive index distribution and an extinction coefficient distribution in the visible light range, and their corresponding coefficients do not have a relatively large difference, to facilitate subsequently an excellent gradient refractive layer being designed through doping.

Through a relevant literature survey, we selected the following materials. M. Ganchev et al.[50] measured that the refractive index of SnO_2 decays gently in the visible light range, and its extinction coefficient begins to approach 0 at 400 nm wavelength. DBR designed and applied with SiO_2 and Ta_2O_5 has good optical properties and can be used as a laser energy focusing device.[51] The k value of SiO_2 and Ta_2O_5 films is almost zero in the optical wavelength range of 300–1000 nm, and is recognized as a lossless dielectric film. The n value is also basically stable with changes in the wavelength. MgF_2 and Nb_2O_5, similar to SiO_2 and Ta_2O_5, are excellent materials for DBR and have low extinction coefficients in the visible range.[52] Through various methods such as PP-PW, it was proved that $Li_2Si_2O_5$ and $Ca_5(PO_4)_3F$ both have certain mechanical and optical properties.[53,54] According to the results of absorption and reflection spectra, the refractive index $n(x)$ spectra of the two compounds increase slowly with the increase of energy in the infrared-visible light region. At low frequency (energy) in the infrared-visible light region, the extinction coefficients of the two compounds are zero, which indicates that LD and FA

This journal is © the Owner Societies 2024

Phys. Chem. Chem. Phys., 2024, 26, 19755–19774 | 19757

Table 1 The refractive index, extinction coefficient and initial thickness of each layer of material

Layer number	0	1	2	3	4
Material name	$SnO_2 \cdot SiO_2$	NTLC	TML	TMC	Glass
Refractive index	1.66	1.86	1.83	1.80	1.5159
Extinction coefficient	0	0.0015	0	0	0
Initial thickness/nm	550	250	50	50	50

are effectively transparent. It also shows that the two compounds are theoretically excellent visible light and infrared transparent materials.

In order to improve the performance of the gradient refractive layer, we doped the above materials to obtain the materials of each layer in the model. The doping formula for refractive index is[55]

$$n_k = \sum n_i x_i \qquad (1)$$

where n_i and x_i represent the refractive index and the molar percentage of the materials, respectively. The extinction coefficient is also calculated using the same method.

The refractive index, extinction coefficient and other parameters of the materials of each layer obtained by the above method are shown in Table 1 below.

2.2. Simulation method

2.2.1 Admittance recursion method. The admittance recursion method is the core method used in this article for assessing the anti-reflective performance of anti-reflective coatings. Widely acknowledged for its efficacy, this method[31,56] has long been mentioned to be of great value for calculating the optical properties of multi-layer transmission films at any angle of incidence with high accuracy. The admittance recursion method is a method used to solve the electromagnetic field vector distribution at the interface between different materials. It can equate the interface between multi-layer dielectric films into one interface through calculation. There is no need to consider the effects of each interface. Consequently, the method is used to iterate the parameters of each film layer

to precisely compute the transmission, reflection, absorption, and other optical parameters of the film system, thereby reducing computational complexity while preserving optical performance.
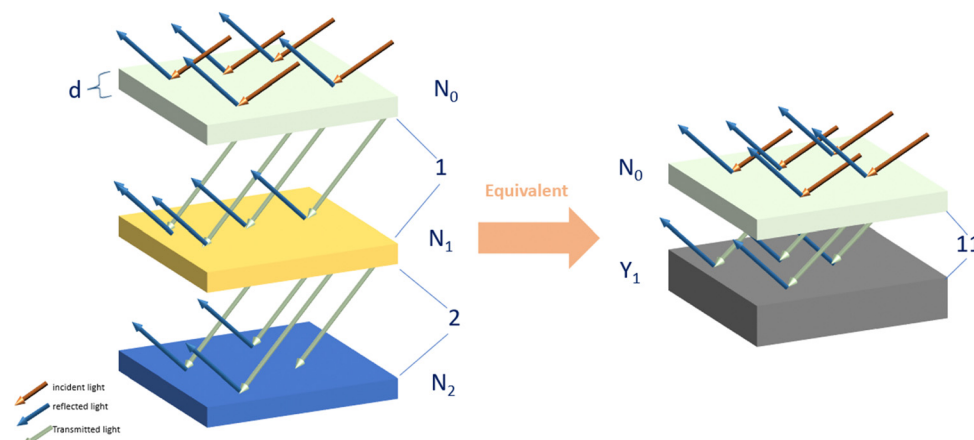
The materials eligible for calculation using the admittance recursion method are categorized into two types: light transmission medium layers and light transmission absorption layers. Given that certain materials chosen in this study possessing extinction coefficients and absorb optical energy, to ensure the rigor of the simulation calculations, this article uses a complex refractive index algorithm for absorbing-type optical transmission layers, which will be elucidated in the subsequent analysis.

Fig. 2 shows the light path diagram of the transmission of a uniform isotropic medium with three layers of thickness d, and the light path diagram of the transmission of two layers of medium simplified by the admittance recursion method. In this context, the admittance of each layer is N_0, N_1, N_2, the interface between N_0 and N_1 is interface 1, and the interface between N_1 and N_2 is interface 2. The equivalent medium admittance is Y_1, and interface 1 and interface 2 are converted into interface 11. According to Fresnel's law reasoning, the reflection coefficient r of the converted model can be obtained as follows:[57,58]

$$r = \frac{N_0 - Y_1}{N_0 + Y_1} \qquad (2)$$

In other words, upon determining the magnitude of Y_1, the entire model's optical properties such as the reflection coefficient of the entire model, can be solved through relevant algorithm equations. The equation and derivation process of the solution are given below Y_1:

At interface 1, the electromagnetic quantity here can be obtained according to Maxwell's equations. However, after passing through N_1, at the same position on interface 2, the state of waves propagating from different directions at different times is determined by the phase factor of the wave. The phase

Fig. 2 Schematic diagram of admittance recursion method.

19758 | *Phys. Chem. Chem. Phys.*, 2024, **26**, 19755–19774

This journal is © the Owner Societies 2024

factor is related to phase thickness φ:[51,59,60]

$$\varphi_1 = \frac{2\pi}{\lambda} \times N_1 \times d = \frac{2\pi}{\lambda} \times (n_1 - \mathrm{i}k_1) \times d \qquad (3)$$

Among them, φ_1 is the phase thickness of the second layer medium, λ represents the wavelength of the incident light, N_1 represents the admittance of the second layer medium, n_1 represents the effective refractive index of the second layer medium, k_1 represents the effective extinction coefficient of the second layer medium, d represents the thickness of the medium layer.

As an electromagnetic wave, sunlight is divided into TM waves and TE waves. The two waves have different effects when calculating the optical properties of the grating structure.[61–63] A. López-Suárez *et al.*[64] experimentally obtained the differences in the nonlinear optical response of Bi–Ag and those of other samples under different pulses and different polarization angles. For TE waves, the electric field is perpendicular to the incident surface and parallel to the grooves of the subwavelength grating, and the interaction mainly involves the interaction of the electric field with the vertical component of the nanostructure. In contrast, for TM waves, where the electric field is parallel to the incident surface and perpendicular to the grating grooves, the interaction involves a stronger interaction of the magnetic field with the horizontal component of the nanostructure. AR optical structures should exhibit high transmittance for both polarization waves within a range of incident angles.[65] We take the rotating paraboloid structure in the initial model as the object to analyze the impact of the incident polarization of TE waves and TM waves, as shown in Fig. 3 below.

From the Fig. 3 above, we can see that both TE waves and TM waves have close to 100% transmittance when the incident angle is small. As the incident angle continues to increase, the curves of the two show an attenuation of approximately exponential profiles. It still has excellent transmission performance of greater than 80% at the incident angle of 80°. This result is
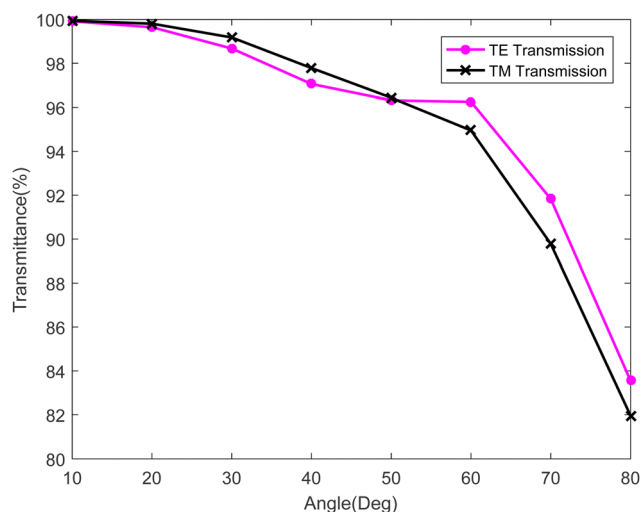

Fig. 3 For the initial rotating paraboloid subwavelength structure, the transmittance of the TE wave and TM wave at 550 nm wavelength in the incident angle range of 10°–80°.

similar to the high-efficiency solar cell anti-reflection film designed by L. Chen *et al.*[65]

The admittance recursive method incorporates these differences by calculating the admittance of each layer based on the specific polarization state of the incident light. This difference is critical when determining the overall reflectance and transmittance of a multilayer structure. In our simulations, we averaged the results for TE and TM polarization, a method that simplifies the analysis to provide an overall perspective on the antireflective properties of coatings.

The intensity of TM waves and TE waves will be affected by the incident angle θ. In order to reduce the degree of influence, we introduce a modified admittance η. For the TM wave, the modified admittance is[66,67]

$$\eta_{1M} = \frac{N_1}{\cos \theta} \qquad (4)$$

For the TE wave modified admittance is[66,67]

$$\eta_{1E} = N_1 \times \cos \theta \qquad (5)$$

According to the boundary conditions of Maxwell's equations, the light transmission matrix can be obtained:[31,51,68]

$$\begin{bmatrix} \cos \varphi_1 & \dfrac{\mathrm{i}}{\eta_1} \sin \varphi_1 \\ \mathrm{i}\eta_1 \sin \varphi_1 & \cos \varphi_1 \end{bmatrix} \qquad (6)$$

At this point, Y_1 can be solved:[60,69]

$$\begin{bmatrix} Y_{11} \\ Y_{12} \end{bmatrix} = \begin{bmatrix} \cos \varphi_1 & \dfrac{\mathrm{i}}{\eta_1} \sin \varphi_1 \\ \mathrm{i}\eta_1 \sin \varphi_1 & \cos \varphi_1 \end{bmatrix} \begin{bmatrix} 1 \\ \eta_2 \end{bmatrix} \qquad (7)$$

Among them, η_2 is the modified admittance of the third layer medium, $\begin{bmatrix} Y_{11} \\ Y_{12} \end{bmatrix}$ is the characteristic matrix of the third layer and second layer medium. At this time:[51]

$$Y_1 = \frac{Y_{12}}{Y_{11}} \qquad (8)$$

After matrix calculation of formulas (3)–(8), we can obtain

$$Y_1 = \frac{\eta_2 \cos \varphi_1 + \mathrm{i}\eta_1 \sin \varphi_1}{\cos \varphi_1 + \mathrm{i}\left(\dfrac{\eta_2}{\eta_1}\right) \sin \varphi_1} \qquad (9)$$

By generalizing this equation, we can get the admittance of the nth interface after going through the admittance recursion method:[36]

$$Y_n = \frac{Y_{n+1} \cos \varphi_n + \mathrm{i}\eta_n \sin \varphi_n}{\cos \varphi_n + \mathrm{i}\left(\dfrac{Y_{n+1}}{\eta_n}\right) \sin \varphi_n} \qquad (10)$$

According to eqn (3), N represents the complex refractive index, which can be obtained through complex processing:

$$Y_n = Y_n' + \mathrm{i}Y_n'' \qquad (11)$$

This journal is © the Owner Societies 2024

Phys. Chem. Chem. Phys., 2024, **26**, 19755–19774 | **19759**

By recursively calculating eqn (10) and (11), we can get the admittance of the first interface after the admittance recursion method:

$$Y_1 = Y_1' + i Y_1'' \tag{12}$$

At this point, the reflection coefficient r can be solved:[36]

$$r = \frac{N_0 - Y_1' - i Y_1''}{N_0 + Y_1' + i Y_1''} \tag{13}$$

reflectivity R:[36]

$$R = r \times \bar{r} = \frac{\left(N_0 - Y_1'\right)^2 + \left(Y_1''\right)^2}{\left(N_0 + Y_1'\right)^2 + \left(Y_1''\right)^2} \tag{14}$$

Because there is absorption caused by the extinction coefficient, the transmittance T is solved using energy flow density. The energy flow density ratio between the nth interface and the $n + 1$th interface is[70,71]

$$E_n = \frac{Y_{n+1}'}{Y_n' \times \left(\cos \varphi_n + i \left(\dfrac{Y_{n+1}}{\eta_n}\right) \sin \varphi_n\right)^2} \tag{15}$$

After the superposition of calculation of formula (15) and removal of the optical loss of reflected light, the transmittance T is

$$T = (1 - R) \times \prod_{n=1}^{k} E_n \tag{16}$$

Given T and R, the optical absorbance A of the model can be calculated:[64]

$$A = 1 - R - T \tag{17}$$

2.2.2 Equivalent medium theory. The admittance recursion method has been deduced in detail in Section 2.2.1 above, but it cannot directly solve the electromagnetic vector distribution of periodic subwavelength structures. Therefore, before calculating the AR performance of the subwavelength structure part, it is necessary to utilize equivalent medium theory to approximate the subwavelength structure as a multilayer film

system. This approximation renders the structure equivalent to a positive planar layer-by-layer arrangement without compromising its optical properties. Maxwell–Garnett theory (MGT) can effectively avoid violations of the electric field continuity condition when solving the Fresnel equation after simplifying the algorithm model.[72] I. V. Lavrov[73] provided a relatively complete derivation and promotion application of Maxwell–Garnett theory, highlighting its reliability in the application of equivalent approximation to irregular media.

As shown in Fig. 4(a), the pyramid subwavelength structure is periodically cut into multiple independent layers of equal height. The refractive index and extinction coefficient of each layer are N_S and K_S, the refractive index and extinction coefficient of the outside air are N_i and K_i. After effective conversion, the effective refractive index of each layer in Fig. 4(b) N_n can be solved according to the equivalent medium theory related equation:[37]

$$N_n = \sqrt{N_S^2 f_n + N_i^2 (1 - f_n)} \tag{18}$$

We derive the extinction coefficient K_n in the same way according to eqn (18):

$$K_n = \sqrt{K_S^2 f_n + K_i^2 (1 - f_n)} \tag{19}$$

Here, f_n is the filling factor of the subwavelength structure.

Because the film layers have thickness, the filling factor will change with the thickness change. When calculating, we choose the middle height of the film layer as the standard to perform equivalent conversion of the subwavelength structure layer by layer.

2.2.3 Gradient refractive index. Gradient refractive index refers to a transmission layer composed of a variety of materials with different refractive indexes, and the refractive index gradually decreases as the incident light propagates, which can effectively reduce broadband anti-reflection. The structural diagram is shown in Fig. 5 below.

According to Snell's law and Fresnel's law[55,74] combined with Fig. 5(a), it can be seen that
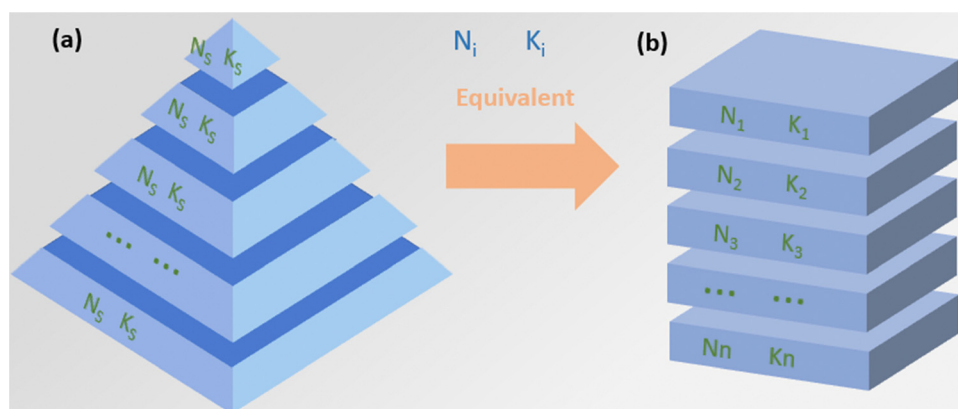
$$n_0 \sin \theta_0 = n_1 \sin \theta_1 \tag{20}$$

Fig. 4 Schematic diagram of equivalent medium theory.

19760 | *Phys. Chem. Chem. Phys.*, 2024, **26**, 19755–19774

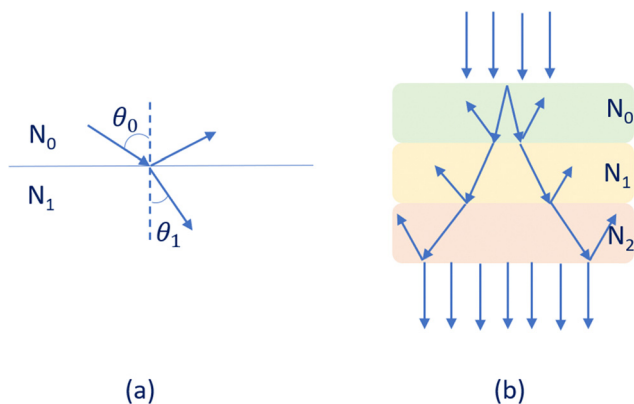This journal is © the Owner Societies 2024

Fig. 5 Gradient refractive index structure diagram: (a) two-layer medium light propagation diagram (b) three-layer gradient medium light propagation diagram.

In the case of normal incidence, its transmittance T and reflectivity R are respectively:[55,74]

$$R = \frac{(n_1 - n_0)^2}{(n_1 + n_0)^2} \tag{21}$$

$$T = \frac{4n_0 n_1}{(n_1 + n_0)^2} \tag{22}$$

By recursion of formula (22), we can get the formula for calculating the transmittance of light when the incident light is incident normally on the a-layer gradient refractive layer:

$$T = \frac{4n_0 n_1}{(n_1 + n_0)^2} \prod_{n=2}^{a} \frac{\frac{4n_n n_{n-1}}{(n_n + n_{n-1})^2}}{1 - \frac{(n_n - n_{n-1})^2}{(n_n + n_{n-1})^2} \times \frac{(n_{n-2} - n_{n-1})^2}{(n_{n-2} + n_{n-1})^2}} \tag{23}$$

Considering the extinction effect of the material, in order to maintain the advantages of the gradient refractive layer and reduce the influence of the extinction coefficient, this paper selects three layers of gradient refractive layers. It can be verified by formula (23) that when the extinction coefficient is ignored, the light transmittance of the gradient refractive layer designed in this paper is 99.25% when the light is incident at the normal angle. This result shows that our design has certain research value, and the gradient refractive layer will be studied and discussed in more depth later.

2.3. Simulation process

The light energy in the model comes from sunlight. The wavelength range of the incident light is 300–800 nm, and the incident angle is 0–80°.

Anti-reflective coatings (ARC) are predominantly influenced by the incident angle θ and wavelength λ of the incident light. Regarding the variation in transmittance of subwavelength structures, different designs and array layouts, such as rotating paraboloid, cylinder, cone, or pyramid structures arranged in different arrays, may result in varying degrees of light capture and absorption. Through the assembly of multiple subwavelength structures, we can explore and identify the optimal configuration. Furthermore, the height of the subwavelength structure plays a key role in determining its effectiveness. By adjusting the height of the structure, we can control the phase shift of incident light, thereby minimizing reflections.

In the optimization of the gradient refractive layer, we have proven the effectiveness of the material we selected in Section 2.2.3. However, due to the existence of the material's extinction coefficient, the change in light transmittance also involves the thickness of each layer. Hence, under different incident conditions, the thickness of each gradient refractive layer must be fine-tuned to ensure optimal light absorption within the spectral range.

By systematically exploring the interplay between the incident angle, wavelength, geometric shape of subwavelength structures and gradient refractive layer thickness, we aim to determine, through simulation and optimization processes, the most effective structural parameters, to maximize the light transmission efficiency of the coating. The simulation process is shown in Fig. 6 below.

2.4. Simulation assumptions

The following are the assumptions made during the modeling process:

(1) The magnetic permeability of all media is assumed to be 1.

(2) The medium of the multi-layer film with a subwavelength structure is uniform, and the two adjacent films are assumed to be parallel to each other.

(3) The model only considers the phenomena of light incidence, reflection, and transmission, as well as light absorption caused by the extinction coefficients of certain materials. Other phenomena such as light attenuation and scattering resulting from interactions between atoms are not taken into account.

3. Results and discussion

We employed the admittance recursion method and equivalent medium theory combined with the idea of gradient refractive index on the MATLAB software platform to successfully simulate the transmittance of sunlight with different incident wavelengths and incident angles in the anti-reflective coating model. Through this approach, we successfully developed an optimization model that could solve problems, such as high reflectivity, narrow absorption spectrum, and low solar energy utilization. This model guarantees optimal overall light transmittance across the specified wavelength and angle ranges.

3.1. Optimization of subwavelength structures

In the model introduction (Section 2.1), the initial subwavelength structures used in this paper have been introduced. We set them up next to each other with an initial height of 550 nm. Among them, the ellipse, cylinder, cone and paraboloid are arranged in the densest hexagonal arrangement, and the cube and pyramid are arranged in the square grid

This journal is © the Owner Societies 2024

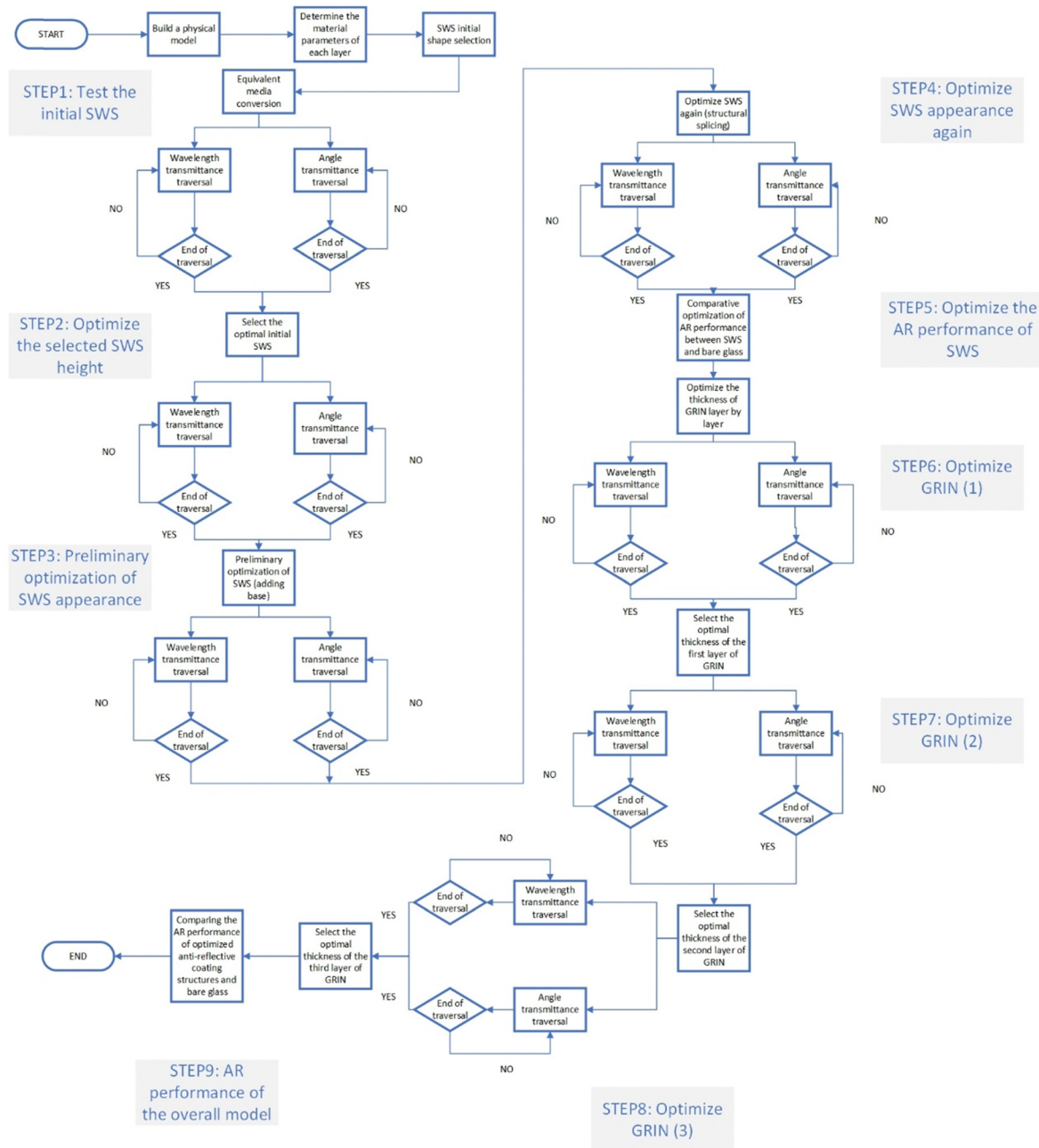*Phys. Chem. Chem. Phys.*, 2024, **26**, 19755–19774 | **19761**

Fig. 6   Anti-reflective coating modeling and optimization flow chart.

arrangement. Table 1 shows the refractive index and extinction coefficient of subwavelength structural materials. The external medium is air. We set the refractive index to 1 and the extinction coefficient to 0.

As the subwavelength structure deviates from a typical planar structure, the admittance recursion method is not directly applicable to solve the electromagnetic vector distribution. Equivalent medium theory should be applied first for equivalence transformation. According to eqn (18) and (19), we calculate the distribution of effective refractive index and effective extinction coefficient relative to the height of each shape, as shown in Fig. 7.

As can be seen from Fig. 7(a), the effective refractive index of the cube and the cylinder basically does not change with the change of height, which makes them have no obvious Fresnel reflection in the body, but the refractive index without gradient makes them have no high comprehensive transmission ability, and both show a large jump when they are in contact with the external air medium, which will produce a strong reflection. Because of the unique shape of the elliptic structure, the distribution of the effective refractive index is like an arch bridge, which increases first and then decreases with the increase of height, and the change amplitude is large. In contrast, the effective refractive index curves of the other three

19762 | *Phys. Chem. Chem. Phys.*, 2024, **26**, 19755–19774

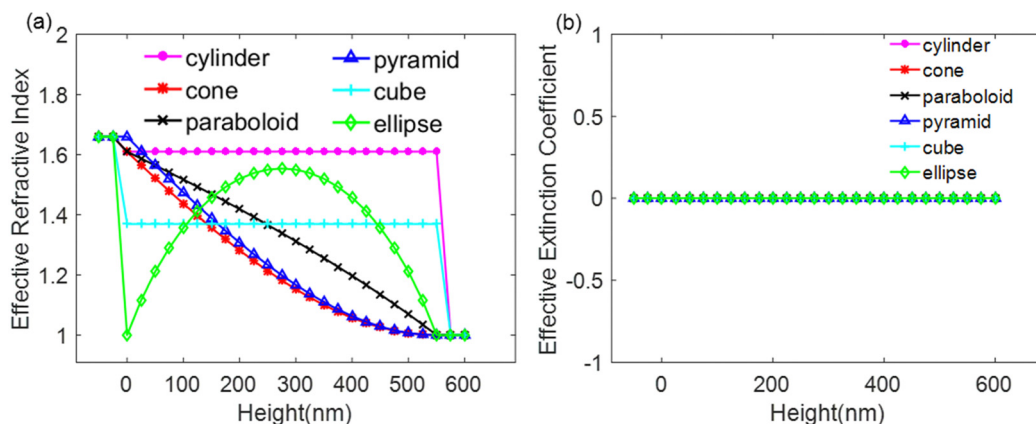This journal is © the Owner Societies 2024

Fig. 7 Distribution diagrams of (a) effective refractive index and (b) effective extinction coefficient of initial structures.

shapes are more gentle, and the formation of gradients improves the ability to reduce Fresnel reflection within the subwavelength structure. As the height gradually decreases, the refractive index curves of cone and rotating parabola shapes show a slight jump during the whole calculation process, while the refractive index curves of pyramid shapes show no obvious jump during the whole calculation process. The reason for the abrupt change is that the base of the conical and rotating paraboloid structures is circular, but they are arranged in the densest hexagonal arrangement, which results in incomplete filling of the bottom of both structures, which will be the focus of subsequent optimization. It can be seen from Fig. 7(b) that at any height, the effective extinction coefficient of all initial structures is 0.

After determining the effective refractive index and effective extinction coefficient of various shapes, we can use the admittance recursion method to gradually calculate the light transmittance of the four initial shapes under incident light, as shown in Fig. 8 below. The minimum wavelength transmittance, average wavelength transmittance, minimum angle transmittance and average angle transmittance of each shape are also given, as shown in Table 2.

From Fig. 8(a) combined with the data in Table 2, it can be seen that within the wavelength range of 300–800 nm of the normal incidence of the incident light, the light transmittivity of the cone, pyramid and paraboloid is close to 100% and exceeds 99.8%. The remaining three structures, cube, ellipse and cylinder, show a tendency to fluctuate with the increase of wavelength in this case, but the change in amplitude of the cylindrical type is smaller.

As can be seen from Fig. 8(b), when the wavelength of incident light is 550 nm, the transmittivity of cone, pyramid and rotating paraboloid is almost perfect in the small incidence angle range. However, with the increase of the incidence angle, the light transmittance of the cone and pyramid structure decreases sharply at about 40°–50°. The structure of the rotating paraboloid shows a slight attenuation trend in the range of 20°–40° and gradually flattens out and then drops sharply at about 60°. The cube and the ellipse in the small angle incidence time transmission effect is not as good as the above three types. The attenuation rate of the elliptical type is the fastest, which begins to decrease rapidly at about 40°, and begins to rise at about 60°. In contrast, the cube has obvious anti-reflection advantages at a large angle of incidence. Although the light
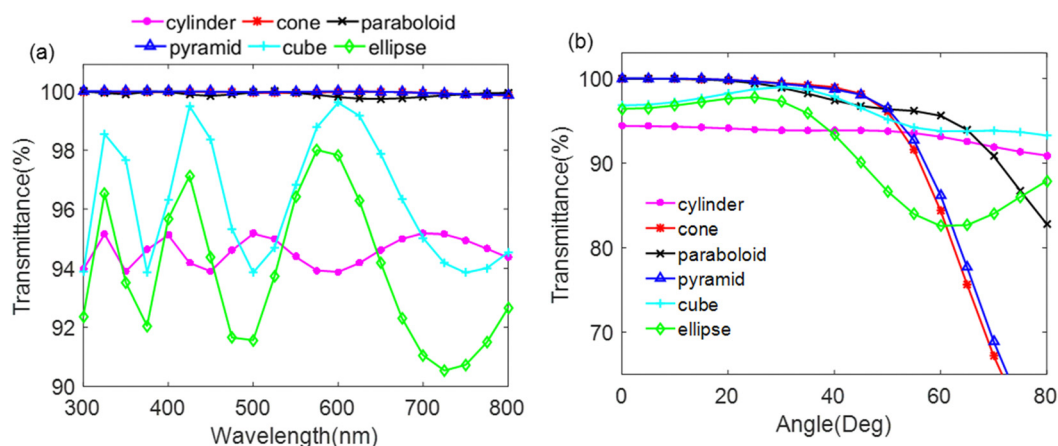

Fig. 8 Subwavelength structures of initial shapes: (a) transmittance variation with incident wavelength under vertical incidence, (b) transmittance variation with incident angle at 550 nm wavelength.

This journal is © the Owner Societies 2024

Phys. Chem. Chem. Phys., 2024, **26**, 19755–19774 | **19763**

Table 2 Specific transmittance for initial subwavelength structures

Type	$T_{wave-ave}$/%	$T_{wave-min}$/%	$T_{angle-ave}$/%	$T_{angle-min}$/%
Cylinder	94.5934	93.8437	93.4487	90.8891
Cone	99.9511	99.8520	90.3499	55.4010
Paraboloid	99.8845	99.7375	96.2796	82.7550
Pyramid	99.9671	99.8683	90.8550	56.0125
Cube	96.3874	93.8437	96.2590	93.2697
Ellipse	93.8796	90.5135	91.2879	82.4118

transmittance of the cylindrical type is slightly lower than that of other shapes at small angles, like the cube structure, it has obvious anti-reflection advantages at large angles of incident light. In dealing with the problem of large-angle light transmission attenuation, the cylinder and the cube have obvious exploitable potential.

Through the analysis of Fig. 8 and Table 2, the incident light transmittance of six initial subwavelength structures is summarized. For full wavelength transmittance at normal incidence, pyramid, cone and rotating paraboloid can be selected. For full angle transmittance of a certain wavelength, we can choose the type of rotating paraboloid, cube, and cylinder. Since our research is to ensure that the antireflection coating is fully optimized in the angle and wavelength range,

the rotating paraboloid with significant advantages in both aspects is finally selected as the basic structure of the subwavelength.

After determining the shape of the basic subwavelength structure, its height needs to be adjusted. Based on the initial height of 550 nm, the height test range is set to unequal intervals of 50–1600 nm. The variation pattern of wavelength reflectivity and angle reflectivity within this range is as shown in Fig. 9.

Observing Fig. 9(a), it's apparent that rotating paraboloid structures of varying heights consistently exhibit high transmittances within the wavelength range, all surpassing 94.5%. Fig. 9(b) shows that the wavelength average transmittance and wavelength minimum transmittance have a rapid growth trend in the height range of 50 nm to 300 nm, and then maintain an excellent transmission effect of more than 99.5%.

Fig. 9(c) indicates that the rotating paraboloid structure has high transmittance at low angles, but it will decrease rapidly as the angle increases. Meanwhile, Fig. 9(d) illustrates that the average transmittance across all angles maintains an effective transmission, fluctuating around 95%. However, notable discrepancies emerge in the minimum angle transmittance concerning the height of the rotating paraboloid structure, among
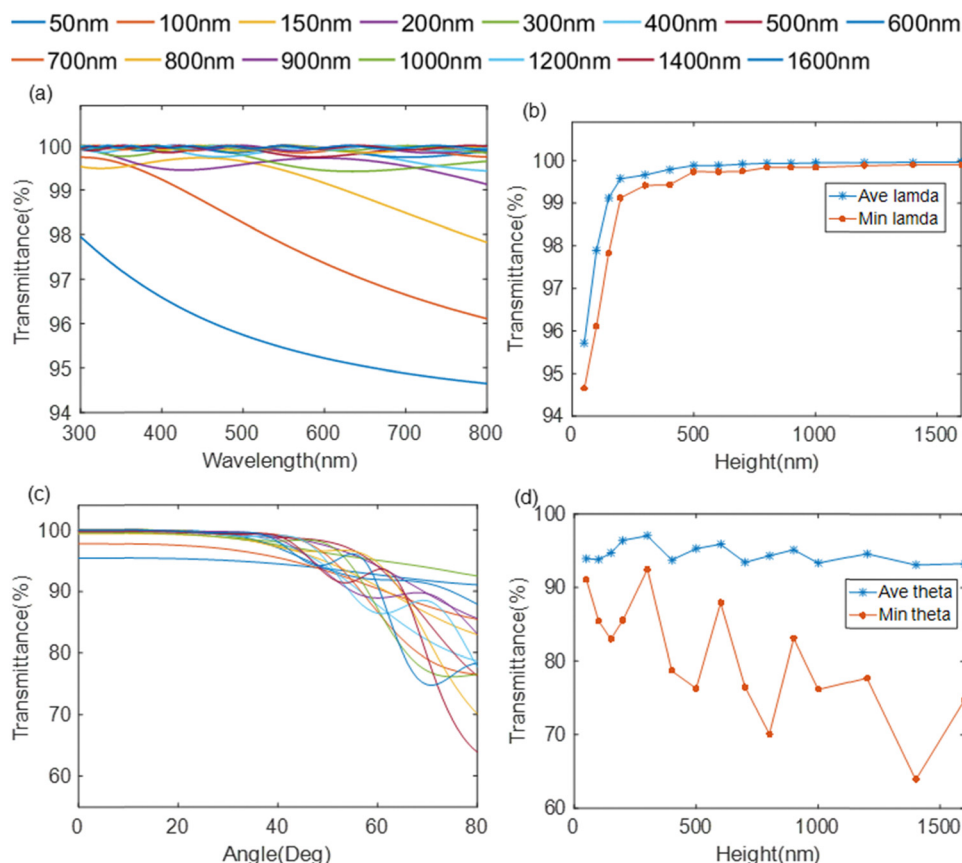

Fig. 9 For rotating paraboloid structures of different heights: under normal incidence: (a) the transmittance varies with incident wavelength. (b) The change of average wavelength transmittance and minimum wavelength transmittance with the height of the rotating paraboloid structure. When the incident wavelength is 550 nm: (c) the transmission varies with the incidence angle. (d) The change of average angle transmittance and minimum angle transmittance with the height of the rotating paraboloid structure.

19764 | *Phys. Chem. Chem. Phys.,* 2024, **26**, 19755–19774

This journal is © the Owner Societies 2024

which the top three transmittance heights are 50 nm (average transmission rate: 93.9372%, minimum transmittance: 91.0448%), 300 nm (average transmittance: 97.0405%, minimum transmittance: 92.4871%) and 600 nm (average transmittance: 95.8907%, minimum transmittance: 87.8929%). Although 300 nm is optimal in the angle range, in order to achieve the comprehensive optimization in the wavelength range and angle range, the height of 600 nm was finally selected.

After determining the height parameters of the subwavelength structure, the shape of the subwavelength structure is modified by shape splicing to improve the AR performance. From the analysis of Fig. 7, the effective refractive index of the rotating paraboloid exhibits a jump at lower heights due to incomplete fitting of its array method to the base. The bottom surface of the rotating paraboloid is circular, and the distribution surface of the array is hexagonal. Although the rotating paraboloids are arranged in a hexagonal grid in an internally tangential circle, its maximum filling rate remains at only 90.7%. Therefore, we add a hexagonal frustum base at the bottom, with its top surface identical to the circular surface of the bottom of the rotating paraboloid, and the bottom surface fully packed with a hexagonally close-packed arrangement. Because the effective refractive index jump range is small,

the height of the added prism is set to one-tenth of the rotating paraboloid structure to ensure that it does not affect the excellent anti-reflective performance of the rotating paraboloid. The shape structure is shown in Fig. 1(g). Because the shape of the model has been changed, the originally set height of 600 nm is not necessarily the optimal height. The height needs to be adjusted again. Considering that the height of the prism is one-tenth of the upper rotating paraboloid structure, we analyze the height of the rotating paraboloid structure as an independent variable, and its height range was the unequal spacing between 200 and 1400 nm. The variation pattern of wavelength transmittance and angle transmittance with the height of the upper half of the rotating paraboloid is shown in Fig. 10 below.

Fig. 10(a) shows that the transmittance of the rotating paraboloid structure with a base in the incident light wavelength range of 300–800 nm is above 99%. It can be seen from Fig. 10(b) that the wavelength average transmittance gradually increases as the height increases, and are all above 99.4%, indicating excellent light transmission characteristics. Although the minimum transmittance does not exhibit as rapid growth as the wavelength-averaged transmittance, and there are instances of flat or even declining curves in between, compared to the original
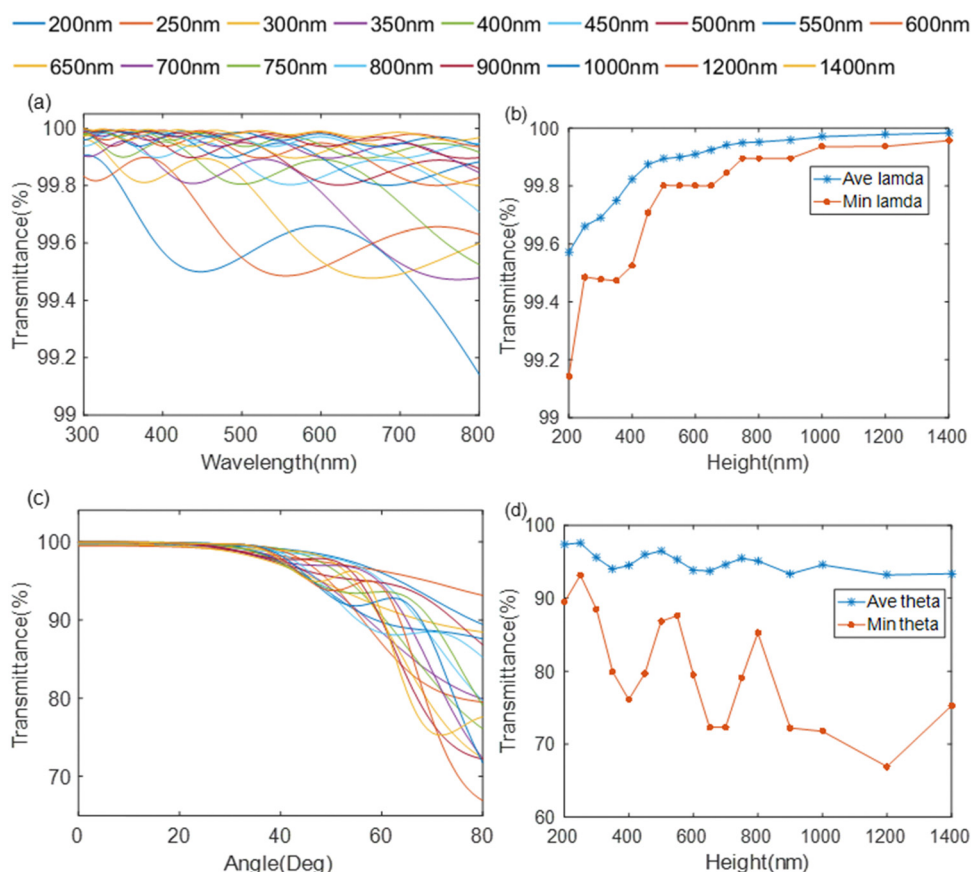

Fig. 10 For rotating paraboloid structures with prism bases of varying heights under normal incidence: (a) transmittance variation with incident wavelength, (b) the change of average wavelength transmittance and minimum wavelength transmittance with the height of the upper part of the structure. When the incident wavelength is 550 nm: (c) transmittance variation with incident angle, (d) the change of average angle transmittance and minimum angle transmittance with the height of the upper part of the structure.

structure, the minimum value of 99.1% still holds a significant advantage. Through the comparison of Fig. 10(a) and (b) with Fig. 9(a) and (b), it can be clearly seen that the subwavelength structure with the base has a significant improvement in wavelength transmittance.

From Fig. 10(c), it can be observed that the rotating paraboloid structure with the base exhibits higher transmittance at small angles compared to Fig. 9(c), showing a significant improvement. However, there is still an issue of rapid decrease with increasing angle, which will be addressed in the following sections. It can be seen from Fig. 10(d) that the angle average transmittance has a good transmission effect in the entire range, basically still fluctuating around 95%, but the angle minimum transmittance has obvious changes with the height of the rotating paraboloid structure. Among these, the heights corresponding to the top four transmittances are 200 nm (average transmittance: 97.4014%, minimum transmittance: 89.4374%), 250 nm (average transmittance: 97.5845%, minimum transmittance: 93.1468%), 300 nm (average transmittance: 95.5698%, minimum transmittance: 88.4663%) and 550 nm (average transmittance: 96.4899%, minimum transmittance: 87.5886%). Considering the angle range, 250 nm appears to be optimal. However, since higher model heights generally result in better transmittance within the wavelength range, we select a height of 550 nm after taking both factors into account. In this case, the base height is set to 55 nm.

Both the basic rotating paraboloid model and the rotating paraboloid model with a prism base have the problem of the sharp decrease in light transmission at large incident angles. Next, we will further optimize the rotating paraboloid model with a prism base that we have designed so far to solve this problem. From the analysis of Fig. 8(b) and Table 2, it can be seen that the cylinder subwavelength structure is obviously superior to the other structural shapes in solving the problem of rapid attenuation of light transmittance in the face of large angle incidence. Since the influence of the angle change of the incident angle on the optical transmission performance mainly occurs at the interface between the top layer and the air

medium, we try to replace part of the top layer of the rotating paraboloid structure in the model with a cylindrical shape, as shown in Fig. 1(h). In order to verify whether this attempt has some value, we splice the four structures of the rotating paraboloid, cylinder, pyramid and cone with the original model in equal proportions, and calculate the changes of their transmittance with the angle when facing the incident wavelength of 550 nm, as shown in Fig. 11 below.

As can be seen from Fig. 11(e), with the increase of the angle after replacing the top layer of the subwavelength structure, the transmission of the cone and pyramid has begun to decay at about 30°, and is below 90% at about 50°. The rotating paraboloid model has some resistance to the attenuation of large angle incidence, which begins to decay at 30° and tends to flatten out at about 60°. Although the cylinder model has a transmittance reduction of about 2% at small angles, it has the best effect at large angle incidence, and the lowest value in the full angle range is as high as 92.99%. From this, it can be concluded that the previous structural transformation scheme for the top layer is of certain value.

After obtaining the shape of the structure, the height ratio between the cylinder and rotating paraboloid structures needs to be adjusted. The height of the rotating paraboloid structure is set as an independent variable for analysis, and its height range is set to equal spacing values between 50 and 500 nm. The variation of wavelength transmittance and angle transmittance with the height of the rotating paraboloid is shown in Fig. 12.

From Fig. 12(a), it can be observed that the transmittance of the optimized model in the incident wavelength range of 300 nm to 800 nm is generally above 95%. Fig. 12(b) shows that with the increase in the height of the rotating paraboloid section, both the wavelength-averaged transmittance and the wavelength minimum transmittance increase.

Fig. 12(c) indicates that the optimized model exhibits no significant changes in transmittance at small incident angles, maintaining above 94% transmittance. However, at large incident angles, compared to the previous model, there is a
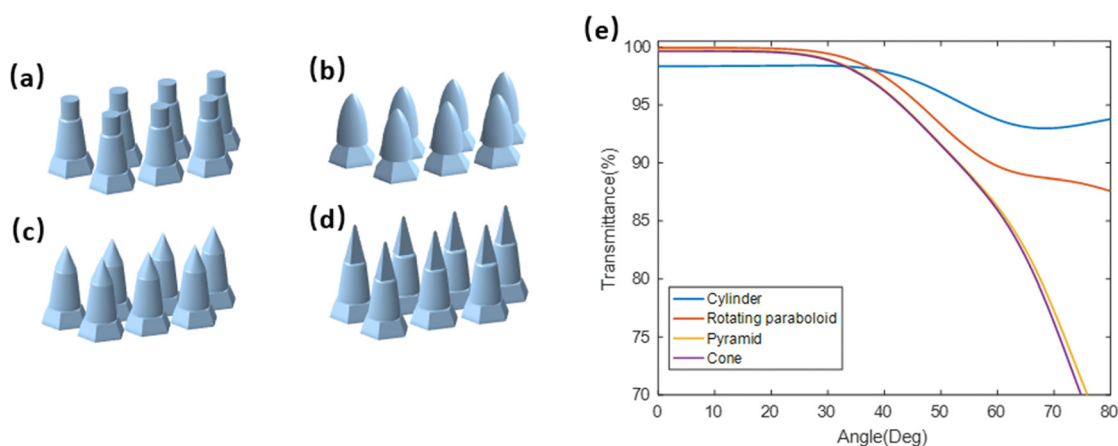

Fig. 11 Subwavelength structure models of four different top-level structures: (a) cylinder, (b) rotating paraboloid, (c) cone, (d) pyramid, and (e) the transmittance varies with the incidence angle at the wavelength of 550 nm.
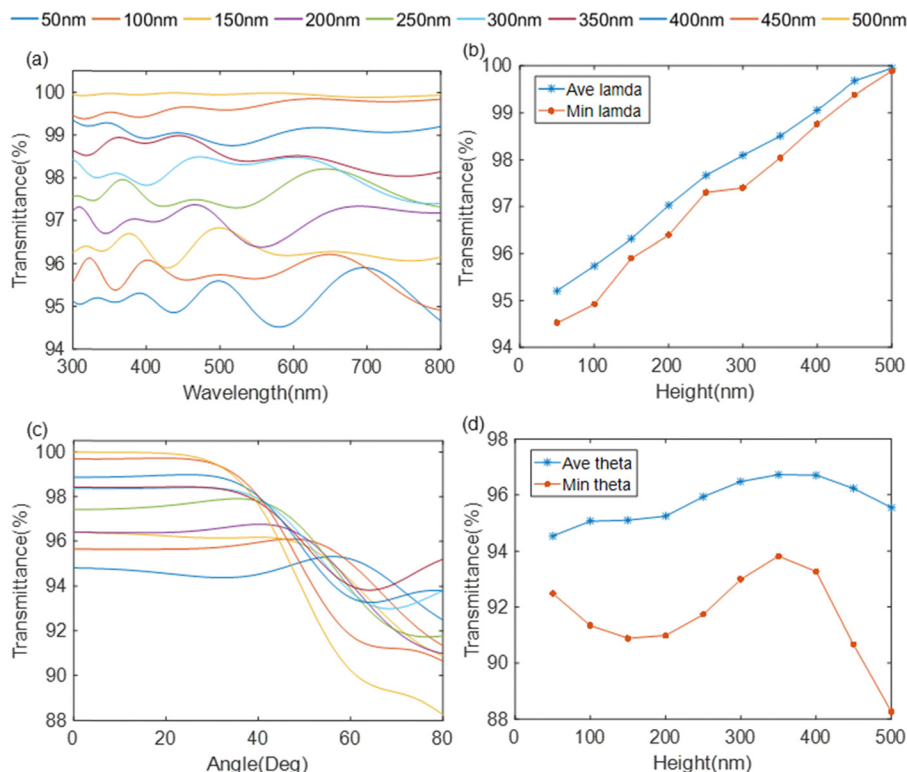
19766 | *Phys. Chem. Chem. Phys.*, 2024, **26**, 19755–19774

This journal is © the Owner Societies 2024

Fig. 12 For the optimized composite structure, under normal incidence: (a) transmittance variation with incident wavelength, (b) variation of wavelength average transmittance and wavelength minimum transmittance with the height of the rotating paraboloid. When the incident wavelength is 550 nm: (c) transmittance variation with incident angle, (d) variation of angle average transmittance and angle minimum transmittance with the height of the rotating paraboloid.

noticeable improvement, greatly enhancing the transmittance, with the minimum value reaching 88.2%. From Fig. 12(d), it can be observed that as the height of the rotating paraboloid section increases, the angle average transmittance shows a fluctuating trend of initially increasing and then decreasing, while the angle minimum transmittance exhibits a pattern of initially decreasing and then increasing. Among these, the top three transmittances are: 300 nm (average transmittance: 96.4839%, minimum transmittance: 92.9937%), 350 nm (average transmittance: 96.7249%, minimum transmittance: 93.8258%), and 400 nm (average transmittance: 96.7100%, minimum

transmittance: 93.2765%). Considering the comprehensive considerations with respect to wavelength, 350 nm is selected. Therefore, the final structure consists of a cylinder top layer with a height of 200 nm, a rotating paraboloid middle layer with a height of 350 nm, and a base layer with a height of 55 nm.

So far, we have completed two structural optimizations of the subwavelength structure. Next, we will compare the optimized subwavelength structure with the bare glass on the same scale. The comparison of the wavelength transmittance and angle transmittance of the two is as shown in Fig. 13. At the same time, the minimum wavelength transmittance, average
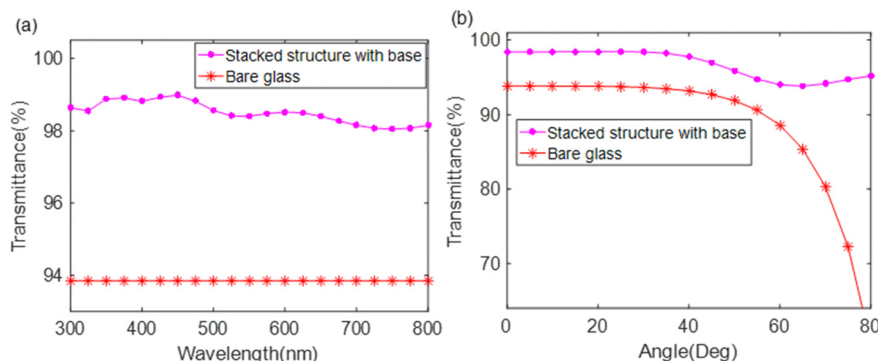

Fig. 13 Comparison between the optimized subwavelength structure model and bare glass: (a) variation of transmittance with incident wavelength under normal incidence, (b) variation of transmittance with incident angle at the incident wavelength of 550 nm.

This journal is © the Owner Societies 2024

Phys. Chem. Chem. Phys., 2024, **26**, 19755–19774 | **19767**

Table 3 Comparison of specific transmittance between optimized subwavelength structure model and bare glass

Type	$T_{wave\text{-}ave}$/%	$T_{wave\text{-}min}$/%	$T_{angle\text{-}ave}$/%	$T_{angle\text{-}min}$/%
Optimization SWS	98.5057	98.0418	96.7249	93.8258
Bare glass	93.8436	93.8436	89.1475	59.1843

wavelength transmittance, minimum angle transmittance and average angle transmittance of the two are given, as shown in Table 3.

The existence of the optimized composite subwavelength structure increases the average transmittance and minimum transmittance within the wavelength range by 4.7% and 3.2% respectively. Moreover, within the angle range, the average transmittance of the glass is increased from 89.1% to 96.7%, and the minimum transmittance has been increased from 59.2% to 93.8%. From this point of view, the application of composite structures can greatly improve the light transmission performance of the outer surface of glass.

3.2. Optimization of the gradient refractive layer

In Section 2.2.3, we have demonstrated the effectiveness of the selected gradient refractive index material at normal incidence without considering the extinction coefficient. Now we begin to

consider the influence of the extinction coefficient, the incident wavelength range of 300 nm–800 nm and the incident angle range of 0°–80° on the light transmission performance of the model to optimize the thickness of each layer of the gradient refractive layer.

In order to ensure the accuracy and rigor of the calculation results, we should fully simulate and calculate the complete process of incident light of different wavelengths and angles incident on the subwavelength structure layer and propagating layer by layer in the three gradient refractive layers below. In Section 3.1, we analyzed and combined the subwavelength structure and obtained the optimized subwavelength array structure model and its light transmission results. In order to simplify the calculation, we ignore the appearance of the subwavelength structure in the following calculations and change it to a positive plane structure of the same size composed of $SnO_2 \cdot SiO_2$. Then, the top layer of planar $SnO_2 \cdot SiO_2$ and the gradient refractive layer below is calculated layer by layer using the admittance recursion method for the optimal light transmission effect in the wavelength range of 300 nm–800 nm and the incident angle range of 0°–80°.

First, we simulate the situation where the incident light passes through $SnO_2 \cdot SiO_2$ and directly irradiates the first layer of NTLC. The initial thickness of NTLC is 250 nm, and the test
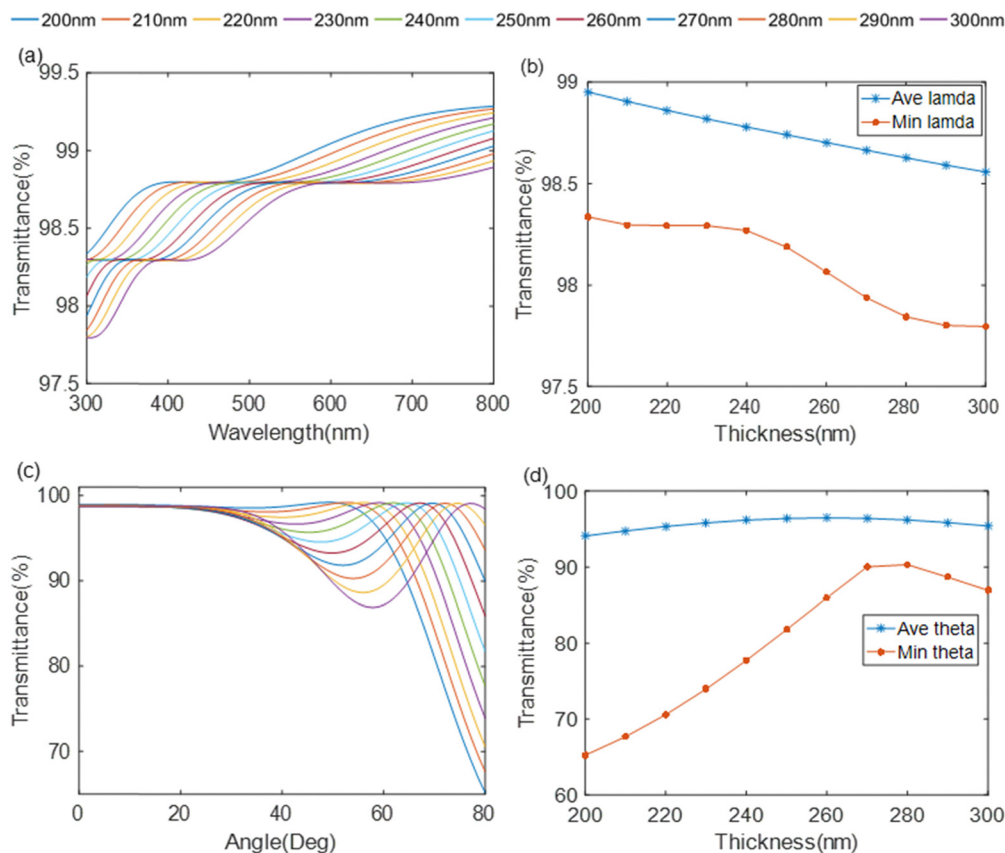

Fig. 14 For NTLC with varying thicknesses: under normal incidence: (a) transmittance variation with incident wavelength, (b) changes in wavelength average transmittance and wavelength minimum transmittance with thickness. When the incident wavelength is 550 nm: (c) transmittance variation with incident angle, (d) changes in angle average transmittance and angle minimum transmittance with thickness.

19768 | *Phys. Chem. Chem. Phys.*, 2024, **26**, 19755–19774

This journal is © the Owner Societies 2024

range is 200–300 nm. The variation of wavelength transmittance and angle transmittance with NTLC thickness is shown in Fig. 14 below.

From Fig. 14(a), it shows that as the incident wavelength increases, the transmittance shows a step-like upward trend, all remaining above 99.7%. However, Fig. 14(b) reflects that as the thickness of NTLC increases, both the wavelength average transmittance and the wavelength minimum transmittance gradually decrease, with the wavelength minimum transmittance decreasing rapidly in the range of 240–270 nm.

Fig. 14(c) indicates that as the incident angle increases, the transmittance shows a trend of first decreasing, then increasing and subsequently experiencing a rapid decline, and there are obvious defects in a large angle range. According to Fig. 14(d), the angle average transmittance remains nearly unchanged at around 95% as the thickness increases, but the minimum angle transmittance first rises and then falls, reaching its peak between 270 nm and 280 nm. Among these, the top three light transmittances are: 270 nm (average transmittance: 96.3985%, minimum transmittance: 90.0054%), 280 nm (average transmittance: 96.1882%, minimum transmittance: 90.3017%) and 290 nm (average transmittance: 95.8458%, minimum transmittance: 88.6515%). Within the angle range, the light transmission properties of 270 nm and 280 nm are almost the same.

Considering the comprehensive wavelength, 270 nm is selected as the final thickness of NTLC.

The light passes through the 270 nm NTLC, and then irradiates onto the TML. The relationship between the thickness of the TML and the wavelength transmittance and angle transmittance is shown in Fig. 15 below.

From Fig. 15(a), it indicates as the incident wavelength increases, the transmittance shows an overall upward trend, and has an excellent transmittance of more than 97.8%. Fig. 15(b) reflects that as the thickness increases, the average transmittance of the wavelength increases slowly, and the minimum transmittance of the wavelength initially rises, then decreases, and eventually stabilizes, all remaining higher than 97.8%.

Fig. 15(c) shows that as the incident angle increases, the transmittance shows a trend of first decreasing and then rapidly increasing. Fig. 15(d) reflects that as the thickness increases, the angle average transmittance slowly decreases but remains at about 95%, while the angle minimum transmittance decreases rapidly. Considering wavelength and angle, the thickness of TML is finally set to 25 nm.

Light transmitted through a 270 nm NTLC and a 25 nm TML will be transmitted to TMC. Before controlling the thickness of TMC, it is necessary to determine the refractive index and
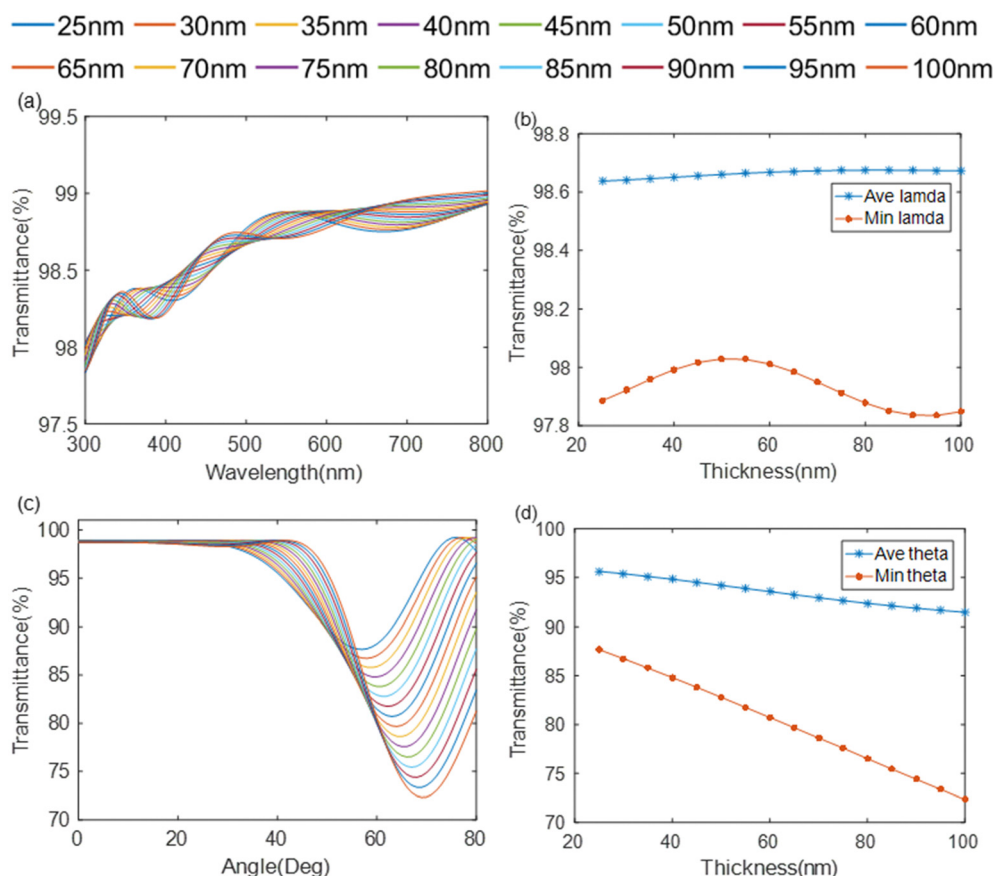

Fig. 15 For TML of various thicknesses, under normal incidence: (a) transmittance variation with incident wavelength, (b) changes in wavelength average transmittance and minimum transmittance with thickness. When the incident wavelength is 550 nm: (c) transmittance variation with incident angle, (d) changes in angle average transmittance and angle minimum transmittance with thickness.

This journal is © the Owner Societies 2024

Phys. Chem. Chem. Phys., 2024, **26**, 19755–19774 | **19769**

extinction coefficient of the underlying dielectric layer. TMC serves as the final layer of the gradient refractive layer, with an absorption layer for photothermal conversion underneath. For simplicity, we use glass as a substitute to calculate the transmittance of the anti-reflective coating (ARC). The relationship diagram of the effect of TMC thickness on wavelength transmittance and angle transmittance is shown in Fig. 16 below.

From Fig. 16(a), it can be observed that as the incident wavelength increases, the transmittance shows a wavy upward trend. Fig. 16(b) reflects that the wavelength average transmittance has high transmittance in the entire thickness range. However, the wavelength minimum transmission initially increases, then decreases, and finally rises again.

It can be seen from Fig. 16(c) that as the incident angle increases, the transmittance shows a trend of first decreasing and then increasing. Fig. 16(d) indicates that with increasing thickness, the average angle transmittance slightly decreases but remains around 90% to 95%, while the minimum angle transmittance decreases rapidly. Taking the wavelength into consideration, the thickness of TMC was ultimately set to 40 nm.

In the above content, we mentioned that the fourth layer of photothermal conversion material is calculated based on conventional glass as a replacement, but in fact, compared with glass, the refractive index of most photothermal conversion materials is higher than the refractive index of the glass, such as CNT[75] (2.63).[76] We modified the refractive index of the fourth layer material by gradient (1.4–2.6) to study the influence of refractive index change of photothermal conversion material on the average wavelength transmittance, minimum wavelength transmittance, average angle transmittance and minimum angle transmittance of the model, as shown in Fig. 17 below.

As can be seen from Fig. 17(a), as the refractive index of the material continues to increase, the average wavelength transmittance and minimum wavelength transmittance both increase first and then decrease, and both reach their peaks at $n = 1.8$, which are 97.2896% and 95.8063% respectively. In the subsequent attenuation process, the attenuation speed of the minimum wavelength transmittance is faster than the average wavelength transmittance, which drops to 87.2458% at $n = 2.6$.

From Fig. 17(b), we can see that with the increasing refractive index of the material, the average angle transmittance and minimum angle transmittance change in a similar way to Fig. 17(a), first increasing and then decreasing. However, the average angle transmittance peaks at $n = 1.6$, which is 95.871%, while the minimum angle transmittance peaks at $n = 1.8$, which
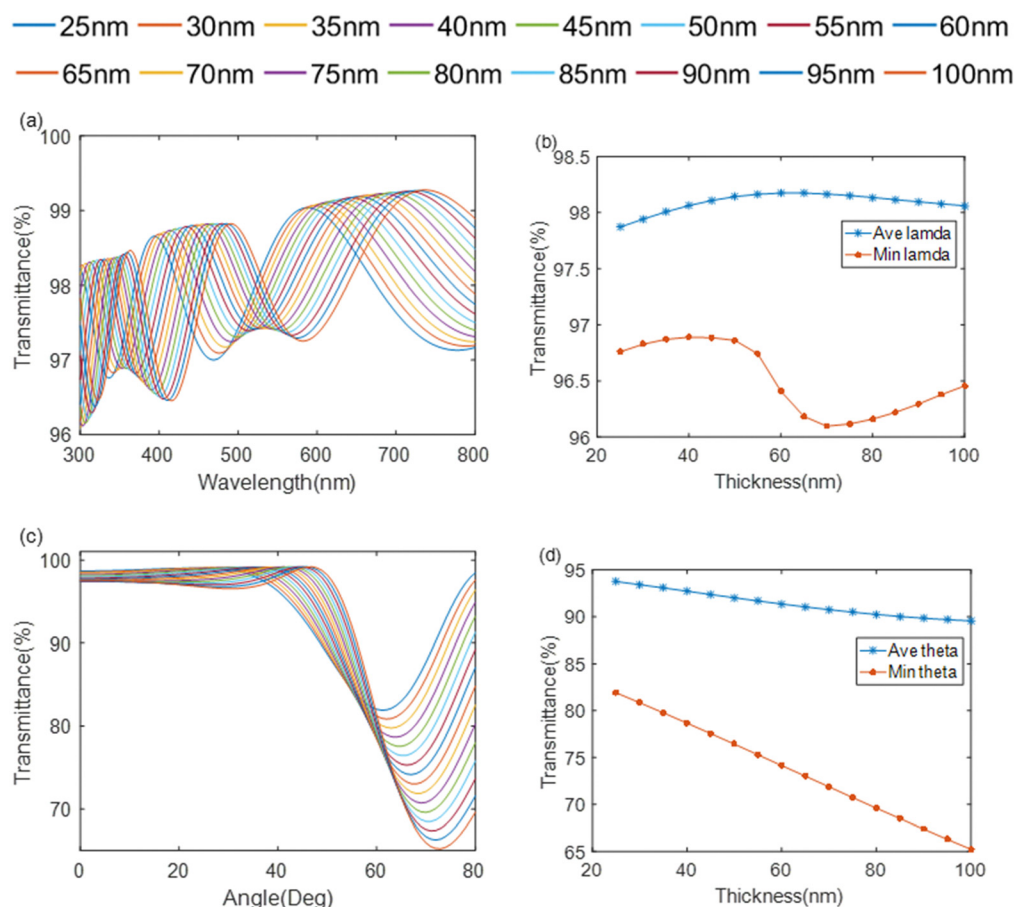

Fig. 16 For TMC with varying thicknesses, under normal incidence: (a) transmittance variation with incident wavelength, (b) changes in wavelength average transmittance and wavelength minimum transmittance with thickness. When the incident wavelength is 550 nm: (c) transmittance variation with incident angle, (d) changes in angle average transmittance and angle minimum transmittance with thickness.
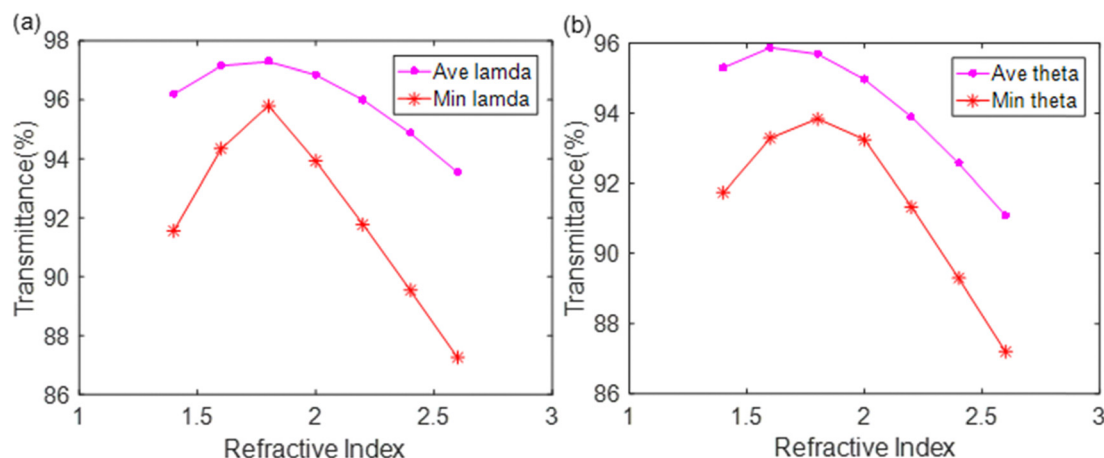
19770 | *Phys. Chem. Chem. Phys.*, 2024, **26**, 19755–19774

This journal is © the Owner Societies 2024

Fig. 17 Effect of refractive index change of photothermal conversion material on (a) wavelength transmittance and (b) angle transmittance of model.
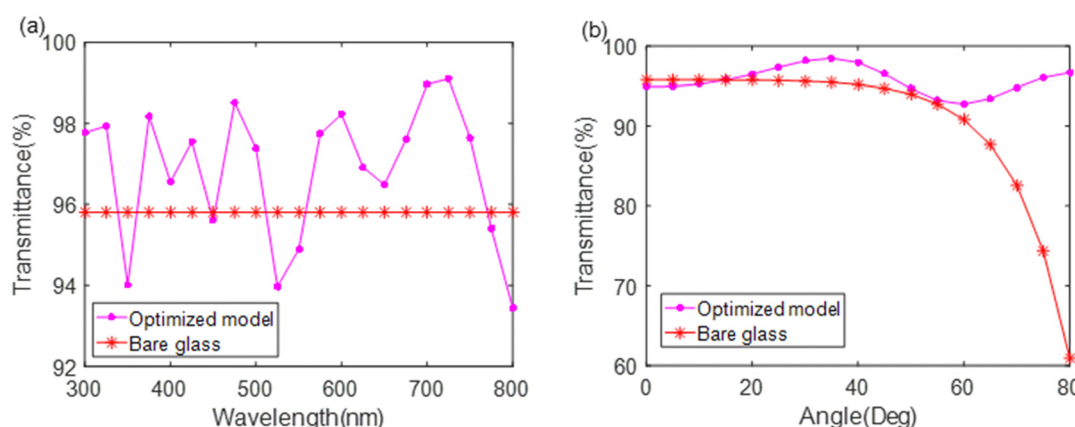

Fig. 18 For the optimized complete transmission layer model compared to bare glass: (a) transmittance variation with incident wavelength under normal conditions, (b) transmittance variation with incident angle at the incident wavelength of 550 nm.

is 93.8450%. In the subsequent attenuation process, the speed of the minimum angle transmittance is higher than the average angle transmittance, which drops to 87.1869% at $n = 2.6$.

It can be seen that the anti-reflection coating designed in this paper has a high tolerance to the refractive index of photothermal conversion materials and can be adapted to a variety of photothermal conversion materials with different refractive indices. Especially when the refractive index of the material belongs to the 1.6–1.8 segment, under the combination of wavelength and angle, it always shows an excellent transmittance of more than 96%.

3.3. AR performance of the overall model after optimization

After the design of 3.1 and 3.2, numerous optimizations have been made to the anti-reflective coating, resulting in the identification of the optimal anti-reflective coating structure. Here, we compare this optimized model structure with bare glass of equal size. The comparison chart of wavelength transmittance and angle transmittance is as shown in Fig. 18. At the same time, the minimum wavelength transmittance, average wavelength transmittance, minimum angle transmittance and

average angle transmittance of both are given, as shown in Table 4.

The existence of the composite structure and gradient refractive layer increases the average transmittance in the wavelength range by 0.7%. In terms of angle range, the average transmittance of the glass is increased from 91.2% to 95.8%, and the minimum transmittance rises from 61.0% to 90.7%. From this point of view, the comprehensive application of composite structures and gradient refractive layers can greatly improve the light transmission performance of the outer surface of glass.

We compare and summarize the results of this study with those of other relevant papers on the anti-reflective performance of anti-reflective coatings in the solar incident wavelength range.

Table 4 Comparison of specific transmittance between optimized complete transmission layer model and bare glass

Type	$T_{wave\text{-}ave}$/%	$T_{wave\text{-}min}$/%	$T_{angle\text{-}ave}$/%	$T_{angle\text{-}min}$/%
Optimization model	96.8668	93.3499	95.7433	92.7641
Bare glass	95.7952	95.7952	91.2130	60.9696

This journal is © the Owner Societies 2024

Phys. Chem. Chem. Phys., 2024, **26**, 19755–19774 | **19771**

Table 5 Comparison of anti-reflection performance of different anti-reflection coatings in the solar wavelength range

Number	Research	Year	Coating structure or material	T (%)
1	This work	2024	Combination of SWS and GRIN	96.3
2	A. B. Trabelsi et al.[77]	2024	SiO_2–ZrO_2 multilayer coating produced by sputtering	94
3	S. Syubaev et al.[78]	2023	Laser engraved nonlinear infrared crystal	84
4	L. Chen et al.[65]	2022	Ring pillar array made of silicon	95.8
5	J. D. Chen et al.[79]	2022	Hexagonal array of transparent silver-based plasma electrodes (A-PME)	82
6	J.-L. Chiang et al.[80]	2021	ITO thin film and four-layer anti-reflection coating deposited on PC substrate	92.25

This illustrates the rationality of the anti-reflective coating design in this study and its ability to increase the incident light transmittance and reduce the light reflection phenomenon caused by interlayer Fresnel reflection during the photothermal process, as shown in Table 5 below.

The transmittance shown in Table 5 of this work is the average of the angle-average transmittance and the wavelength-average transmittance to ensure the overall transmittance of the incident light within the angle range and wavelength range. Some research[65] on antireflective coatings aims to suppress the reflectivity of incident light. In order to unify the form of contrast, we convert it to the form of transmittance, and the sum of the two is one.

From Table 5 above, we can see that the anti-reflection coating designed in this study with the combined application of subwavelength structure and gradient refractive layer greatly improves the light transmission ability compared with the previous anti-reflection coating design research. For example, compared with study [2] and study [6], our simulation result shows that the application of gradient refractive index in the design of anti-reflection layer has a certain effect compared with the discrete gradient anti-reflection film. Compared with study [3], the surface structure we designed becomes more efficient by laser engraving of the surface of the material to improve the anti-reflection ability. Compared with study [5], although both are subwavelength array structures, the transmittance of the laminated fluorescent glass is higher than that of the metal transparent electrode.

It is worth noting that our study [1] and study [4] are similar in terms of transmittance values. Detailed comparison shows that both methods use the reflection suppression performance of the subwavelength structure as the design starting point for model optimization and simulation calculation. In study [4], surface relief AR structures composed of two-dimensional arrays with subwavelength ring and columnar characteristics were used to suppress light reflection. Our design combines an innovative combination of multi-shape stacked splices of subwavelength structures and graded refractive indices to deliver higher performance. Compared with study [4], the influence of the incident angle on the transmittance of the model is discussed in detail in this paper. From the aspect of material selection, doping method is also used to obtain the optimal material parameters. Considering the wavelength range and angle range, the optimized antireflection coating model was designed by splicing the model structure and adjusting the model parameters. It highlights the innovation of our design.

4. Conclusion

In this work, we use the admittance recursion method algorithm combined with equivalent medium theory and gradient refractive index ideas to design and optimize anti-reflective coatings for photothermal conversion. Combining the subwavelength structure and the gradient refractive layer to enhance the transmission capability of the transmission layer, the transmission layer can significantly reduce reflection, increase transmission. This approach improves the solar energy utilization of gradient refractive index fluorescent glass and offers higher efficiency for photothermal conversion devices under light incidence. Ultimately, an anti-reflective coating composed of 605 nm subwavelength structure, 270 nm NTLC, 25 nm TML and 40 nm TMC was designed. Under normal incidence conditions, the coating achieves an average light transmittance of 96.87% within the wavelength range of 300–800 nm. When illuminated with incident light at 550 nm, it reaches an average angle transmittance of 95.74% and a minimum angle transmittance of 92.76% within the angle range of 0–80°. This structural model can effectively address the challenge of inefficient light absorption during photothermal conversion. It outperforms bare glass in terms of light absorption across a wider wavelength range and under large incident angles, making it suitable for various photothermal conversion applications and contributing to improved conversion efficiency.

Data availability

The data that support the findings of this study are available from the corresponding author upon reasonable request.

Conflicts of interest

There are no conflicts to declare.

Acknowledgements

19772 | *Phys. Chem. Chem. Phys.*, 2024, **26**, 19755–19774

This journal is © the Owner Societies 2024

References

1 R. Y. Li, L. B. Zhang, L. Shi and P. Wang, *ACS Nano*, 2017, **11**, 3752–3759.

2 S. D. Stranks and H. J. Snaith, *Nat. Nanotechnol.*, 2015, **10**, 391–402.

3 L. Tang, K.-H. Tsui, S.-F. Leung, Q. Zhang, M. Kam, H.-P. Wang, J.-H. He and Z. Fan, *J. Semicond.*, 2019, **40**, 042601.

4 X. B. Chen, S. H. Shen, L. J. Guo and S. S. Mao, *Chem. Rev.*, 2010, **110**, 6503–6570.

5 E. P. Bandarra, O. S. H. Mendoza, C. L. L. Beicker, A. Menezes and D. S. Wen, *Energy Convers. Manage.*, 2014, **84**, 261–267.

6 H. Chen, F. Wang, K. X. Wang, Y. D. Wu and C. S. Guo, *J. Colloid Interface Sci.*, 2022, **624**, 296–306.

7 C. B. Zhang, C. Yan, Z. J. Xue, W. Yu, Y. D. Xie and T. Wang, *Small*, 2016, **12**, 5320–5328.

8 G. Ni, N. Miljkovic, H. Ghasemi, X. P. Huang, S. V. Boriskina, C. T. Lin, J. J. Wang, Y. F. Xu, M. M. Rahman, T. J. Zhang and G. Chen, *Nano Energy*, 2015, **17**, 290–301.

9 A. E. Kabeel and S. A. El-Agouz, *Desalination*, 2011, **276**, 1–12.

10 W. Z. Ren, Y. Yan, L. Y. Zeng, Z. Z. Shi, A. Gong, P. Schaaf, D. Wang, J. S. Zhao, B. B. Zou, H. S. Yu, G. Chen, E. M. B. Brown and A. G. Wu, *Adv. Healthcare Mater.*, 2015, **4**, 1526–1536.

11 H. N. Wang and S. L. Zou, *Proc. Soc. Photo-Opt. Instrum. Eng.*, 2008, **7033**, S331.

12 S. B. Khan, H. Wu, Z. Xie, W. Wang and Z. Zhang, *ACS Appl. Mater. Interfaces*, 2017, **9**, 36327–36337.

13 B. M. Chaya, P. K. Pattnaik and K. Narayan, *J. Nanoelectron. Optoelectron.*, 2020, **15**, 425–431.

14 A. K. Loganathan, A. A. Stonier and Y. U. Maheswari, *J. Mater. Sci.: Mater. Electron.*, 2021, **32**, 1242–1257.

15 J. W. Leem, D. H. Joo and J. S. Yu, *Sol. Energy Mater. Sol. Cells*, 2011, **95**, 2221–2227.

16 F. Maudet, B. Lacroix, A. J. Santos, F. Paumier, M. Paraillous, S. Hurand, A. Corvisier, C. Dupeyrat, R. García, F. M. Morales and T. Girardeau, *Acta Mater.*, 2020, **188**, 386–393.

17 Z. Q. Lin, G. G. Wang, J. L. Tian, L. Y. Wang, D. D. Zhao, Z. Liu and J. C. Han, *Nanotechnology*, 2018, **29**, 055302.

18 C. Y. Lin, K. Y. A. Lin, T. W. Yang, Y. C. Chen and H. T. Yang, *J. Colloid Interface Sci.*, 2017, **490**, 174–180.

19 T. Tamura, M. Umetani, K. Yamada, Y. Tanaka, K. Kintaka, H. Kasa and J. Nishii, *Appl. Phys. Express*, 2010, **3**, 112501.

20 T. Yeamsuksawat, Y. Morishita, J. Shirahama, Y. T. Huang, T. Kasuga, M. Nogi and H. Koga, *Chem. Mater.*, 2022, **34**, 7379–7388.

21 C. Li, M. Zhang, H. Xu, Y. Tan, Y. Shi and D. Dai, *PhotoniX*, 2021, **2**, 1–35.

22 S. H. Chao, L. H. Yeh, R. T. Wu, K. Kawagishi and S. C. Hsu, *RSC Adv.*, 2020, **10**, 16284–16290.

23 L. Sisken, C. Smith, A. Buff, M. Kang, K. Chamma, P. Wachtel, J. D. Musgraves, C. Rivero-Baleine, A. Kirk and M. Kalinowski, *Opt. Mater. Express*, 2017, **7**, 3077–3092.

24 S. Kitamura, Y. Kanno, M. Watanabe, M. Takahashi, K. Kuroda and H. Miyata, *ACS Photonics*, 2014, **1**, 47–52.

25 Y. Kang, J. Wang, Y. K. Zhao, X. D. Zhao, H. Z. Tao and Y. S. Xu, *Materials*, 2023, **16**, 2566.

26 K. A. Richardson, M. Kang, L. Sisken, A. Yadav, S. Novak, A. Lepicard, I. Martin, H. Francois-Saint-Cyr, C. M. Schwarz, T. S. Mayer, C. Rivero-Baleine, A. J. Yee and I. Mingareev, *Opt. Eng.*, 2020, **59**, 112602.

27 Y.-Y. Yeh, C.-H. Shen and C.-F. Chen, *Appl. Sci.*, 2020, **10**, 2966.

28 H. Li, P. Wang, Y. Zhuo, X. Cao and D. H. Xiong, *J. Am. Ceram. Soc.*, 2020, **103**, 5056–5066.

29 M. Choi, J. W. Leem and J. S. Yu, *RSC Adv.*, 2015, **5**, 25616–25624.

30 X. Li, J. Gao, L. Xue and Y. Han, *Adv. Funct. Mater.*, 2010, **20**, 259–265.

31 H. Liang, Z. Zhang, P. Li, N. Suo and M. Zhang, *Sci. Sin. Technol.*, 2015, **46**, 46–53.

32 N. T. Liu and Y. Q. Jin, *Wave Random Complex*, 2021, **31**, 1921–1930.

33 S. Zare, R. Pouria and S. Edalatpour, *J. Quant. Spectrosc. Radiat. Transfer*, 2021, **261**, 107482.

34 I. A. Starkov and A. S. Starkov, *Int. J. Solids Struct.*, 2020, **202**, 226–233.

35 Y. Wang, J. Shi, X. Liu, B. Chen and X. Wang, *Phys. Chem. Chem. Phys.*, 2024, **26**, 10850–10867.

36 Y. Yin, Y. Bu and X. Wang, *Phys. B*, 2020, **580**, 1092.

37 H. Lin, M. Ouyang, B. Chen, Q. Zhu, J. Wu, N. Lou, L. Dong, Z. Wang and Y. Fu, *Coatings*, 2018, **8**, 360.

38 M. J. Minot, *JOSA*, 1976, **66**, 515–519.

39 H. M. Branz, V. E. Yost, S. Ward, K. M. Jones, B. To and P. Stradins, *Appl. Phys. Lett.*, 2009, **94**, 231121.

40 W. Zhou, M. Tao, L. Chen and H. Yang, *J. Appl. Phys.*, 2007, **102**, 103105.

41 R. Bräuer and O. Bryngdahl, *Appl. Opt.*, 1994, **33**, 7875–7882.

42 M. Abe and M. Koshiba, *JOSA A*, 1994, **11**, 2038–2044.

43 Y. Chen, G. Liu, K. Huang, Y. Hu, X. Zhang and Z. Cai, *Opt. Commun.*, 2013, **311**, 100–106.

44 D. H. Wan, H. L. Chen, S. Y. Chuang, C. C. Yu and Y. C. Lee, *J. Phys. Chem. C*, 2008, **112**, 20567–20573.

45 J. Y. Park, B. J. Kim, C. J. Yoo, W. J. Dong, I. Lee, S. Kim and J.-L. Lee, *Sci. Rep.*, 2020, **10**, 5540.

46 Y. Song, K. Kim, K. Choi, B. Ki and J. Oh, *Sol. Energy*, 2016, **135**, 291–296.

47 X. Cui, Q. Ruan, X. Zhuo, X. Xia, J. Hu, R. Fu, Y. Li, J. Wang and H. Xu, *Chem. Rev.*, 2023, **123**, 6891–6952.

48 M. Kraus, Z. Diao, K. Weishaupt, J. P. Spatz, K. Täschner, H. Bartzsch, R. Schmittgens and R. Brunner, *Opt. Express*, 2019, **27**, 34655–34664.

49 X. Ruan, W. Dai, W. Wang, C. Ou, Q. Xu, Z. Zhou, Z. Wen, C. Liu, J. Hao and Z. Guan, *Nanophotonics*, 2021, **10**, 1683–1690.

50 M. Ganchev, A. Katerski, S. Stankova, J. Eensalu, P. Terziyska, R. Gergova, G. Popkirov and P. Vitanov, *J. Phys.: Conf. Ser.*, 2019, **1186**, 012027.

51 K.-H. Chen, W. Chien, C.-F. Yang and N. Wu, *Sens. Mater.*, 2022, **34**, 2253–2262.

This journal is © the Owner Societies 2024

Phys. Chem. Chem. Phys., 2024, **26**, 19755–19774 | **19773**

52 D. Yong, B. S. Chen, J. J. Lin, H. W. Tseng, Y. L. Wu and C. F. Yang, *Mod. Phys. Lett. B*, 2021, **35**, 2140001.

53 Z. Biskri, H. Rached, M. Bouchear, D. Rached and M. Aida, *J. Electron. Mater.*, 2016, **45**, 5082–5095.

54 Z. E. Biskri, H. Rached, M. Bouchear and D. Rached, *J. Mech. Behav. Biomed. Mater.*, 2014, **32**, 345–350.

55 X. Liu, D. Han, X. Mao, J. Zhang, H. Ren, H. Lin and S. Wang, *J. Eur. Ceram. Soc.*, 2022, **42**, 3579–3585.

56 J. A. Berning and P. H. Berning, *JOSA*, 1960, **50**, 813–815.

57 T. Yamada, H. Nakamura, T. Sugiura, K. Sakuta and K. Kurokawa, *Sol. Energy Mater. Sol. Cells*, 2001, **67**, 405–413.

58 M. Hentschel and H. Schomerus, *Phys. Rev. E: Stat., Non-linear, Soft Matter Phys.*, 2002, **65**, 045603.

59 A. Kozar, *Moscow Univ. Phys. Bull.*, 2018, **73**, 638–643.

60 Y.-C. Chen, C.-F. Yang and E.-Y. Hsueh, *J. Electrochem. Soc.*, 2010, **157**, H987.

61 H.-J. Zhao, S.-L. Yang, D. Zhang, K.-Y. Liang, Z.-F. Cheng and D.-P. Shi, *Acta Phys. Sin.*, 2009, **58**, 6236–6242.

62 H. Zhanhua, M. Xiaoqing, Z. Pan, Z. Yanan, C. Huaiyu and Z. Yinxin, *Opto-Electron. Eng.*, 2017, **44**, 663–669.

63 J. Zhang, T. M. Li, K. T. Huo, M. F. He, C. P. Yin and F. Wu, *Phys. Lett. A*, 2023, **477**, 128885.

64 A. López-Suárez, C. Torres-Torres, B. Can-Uc, R. Rangel-Rojo, C. E. Valencia and A. Oliver, *JOSA B*, 2015, **32**, 805–811.

65 L. Chen and Z. Huang, *Int. J. Opt.*, 2022, **2022**, 9963336.

66 A. Sakurai, H. Tanikawa and M. Yamada, *J. Quant. Spectrosc. Radiat. Transfer*, 2014, **132**, 80–89.

67 C.-W. Yu and Y.-J. Jen, *Opt. Express*, 2010, **18**, 7982–7993.

68 S. Lian, Y. Yu, S. Lin, G. Lin, C. Xu and J. Wang, *Mater. Sci.*, 2017, **7**(1), 78–87.

69 H. A. Macleod and H. A. Macleod, *Thin-film optical filters*, CRC press, 2010.

70 P. Dolganov, K. Baklanova and V. Dolganov, *Liq. Cryst.*, 2020, **47**, 231–237.

71 A. Madani and S. R. Entezar, *Phys. B*, 2013, **431**, 1–5.

72 B. Chen, W. Lu, P. Li, X. Yang, J. Li, K. Huang, J. Kang and R. Zhang, *Opt. Express*, 2022, **30**, 22700–22711.

73 I. V. Lavrov, *Semiconductors*, 2023, **57**, 31–45.

74 L. Shui, Y. Liu and X. Chen, *Int. J. Solids Struct.*, 2018, **143**, 18–28.

75 Y. Liu, Z. Lin, P. Wang, F. Huang and J.-L. Sun, *Nanomaterials*, 2022, **12**, 1101.

76 M. Kurban, *Optik*, 2018, **172**, 295–301.

77 A. B. Trabelsi, G. V. Kaliyannan, R. Gunasekaran, R. Rathanasamy, S. K. Palaniappan, F. H. Alkallas, W. B. Elsharkawy and A. M. Mostafa, *J. Mater. Res. Technol.*, 2024, **28**, 1475–1482.

78 S. Syubaev, E. Modin, S. Gurbatov, A. Cherepakhin, A. Dostovalov, A. Tarasova, P. Krinitsin, A. Yelisseyev, L. Isaenko and A. Kuchmizhak, *Appl. Phys. Lett.*, 2023, **123**, 061108.

79 J. D. Chen, L. Li, C. C. Qin, H. Ren, Y. Q. Li, Q. D. Ou, J. J. Guo, S. J. Zou, F. M. Xie and X. Liu, *InfoMat*, 2022, **4**, e12285.

80 J.-L. Chiang, S.-W. Li, B. K. Yadlapalli and D.-S. Wuu, *Vacuum*, 2021, **186**, 110046.